

High-resolution grids of hourly meteorological variables for Germany

S. Krähenmann¹ · A. Walter¹ · S. Brienens¹ · F. Imbery² · A. Matzarakis³

Received: 18 May 2016 / Accepted: 10 November 2016 / Published online: 28 December 2016
© The Author(s) 2016. This article is published with open access at Springerlink.com

Abstract We present a 1-km² gridded German dataset of hourly surface climate variables covering the period 1995 to 2012. The dataset comprises 12 variables including temperature, dew point, cloud cover, wind speed and direction, global and direct shortwave radiation, down- and up-welling longwave radiation, sea level pressure, relative humidity and vapour pressure. This dataset was constructed statistically from station data, satellite observations and model data. It is outstanding in terms of spatial and temporal resolution and in the number of climate variables. For each variable, we employed the most suitable gridding method and combined the best of several information sources, including station records, satellite-derived data and data from a

regional climate model. A module to estimate urban heat island intensity was integrated for air and dew point temperature. Owing to the low density of available synop stations, the gridded dataset does not capture all variations that may occur at a resolution of 1 km². This applies to areas of complex terrain (all the variables), and in particular to wind speed and the radiation parameters. To achieve maximum precision, we used all observational information when it was available. This, however, leads to inhomogeneities in station network density and affects the long-term consistency of the dataset. A first climate analysis for Germany was conducted. The Rhine River Valley, for example, exhibited more than 100 summer days in 2003, whereas in 1996, the number was low everywhere in Germany. The dataset is useful for applications in various climate-related studies, hazard management and for solar or wind energy applications and it is available via doi:[10.5676/DWD_CDC/TRY_Basis_v001](https://doi.org/10.5676/DWD_CDC/TRY_Basis_v001).

Electronic supplementary material The online version of this article (doi:[10.1007/s00704-016-2003-7](https://doi.org/10.1007/s00704-016-2003-7)) contains supplementary material, which is available to authorized users.

✉ S. Krähenmann
Stefan.Kraehenmann@dwd.de

A. Walter
Andreas.Walter3@dwd.de

S. Brienens
Susanne.Brienens@dwd.de

F. Imbery
Florian.Imbery@dwd.de

A. Matzarakis
Andreas.Matzarakis@dwd.de

¹ Climate and Environment Consultancy Department, Deutscher Wetterdienst, Frankfurter Straße 135, 63067 Offenbach, Germany

² Climate Monitoring Department, Deutscher Wetterdienst, Frankfurter Straße 135, 63067 Offenbach, Germany

³ Research Centre Human Biometeorology, Deutscher Wetterdienst, Stefan-Meier-Straße 4, 79104 Freiburg, Germany

1 Introduction

Gridded climate datasets are required for numerous purposes in applied and theoretical climate and environmental sciences. These include climate change studies (e.g. Goddard et al. 2001), climate model evaluation (Krähenmann et al. 2013), forestry, agriculture and renewable energy applications (Cros et al. 2006; Cannon et al. 2014), for example. Mostly, the required grid spacing of climate variables increases in line with the resolution of analysis. For evaluations at country level, data with a high spatial (grid spacing <5 km) and temporal (sub-daily) resolution are required so that climate and climate-driven variations can be sufficiently well identified (Schär et al. 1998).

The importance of gridded datasets generated by reanalysis methods in climatological studies is steadily increasing (e.g. Mitchell et al. 2004; Cannon et al. 2014). These methods use forecast models and data assimilation systems to reanalyse

archived observations (Dee et al. 2011; Uppala et al. 2005). A reanalysis typically extends over several decades or longer, and covers the entire globe from the Earth's surface to well above the stratosphere. The benefits of reanalysis data sets are the physical consistency of the calculated variables and spatial information of meteorological variables with low density in situ measurements. However, due to high computation time, it is still not possible to calculate reanalysis data sets with high temporal and spatial resolution as required in this study. In most cases, such datasets either cover a long time period with low spatial resolution (e.g. Hersbach et al. 2015) or have the benefit of high spatial resolution with, however, limited time coverage (e.g. Landelius et al. 2016).

Several statistically derived grids of daily climate variables have been published in recent decades, covering areas ranging from small regions to global. Early datasets (Piper and Stewart 1996; Caesar et al. 2006) had a spatial resolution of 1° or coarser. The gridding of high-resolution daily datasets is, however, needed to monitor extreme weather situations (Herrera et al. 2012). Factors such as network density, local topography and the physical behaviour of the climate variable affect the choice of the interpolation method. Over regions of complex terrain and sparse data coverage, gridding is most successful when the applied methodology captures terrain effects (Daly 2006; Frei 2014). Co-variables derived from elevation data are widely used to account for topographic effects (Stahl et al. 2006; Krähenmann et al. 2011).

Frick et al. (2014) generated the HYRAS dataset which comprises gridded daily air temperature and relative humidity for Germany and the hydrological catchment areas of the rivers Rhine, Elbe, Oder and part of the Danube at a horizontal resolution of 5 km, covering the period 1951–2006. Optimal interpolation (Gandin 1965) was applied in order to interpolate both air and dew point temperature, and relative humidity was subsequently derived from the two datasets.

A number of high-resolution wind maps for Germany have also been created (Gerth and Christopher 1994; Walter et al. 2006). Walter et al. (2006) produced a monthly wind speed dataset of 1-km² resolution using a two-step approach. Firstly, they derived a background field through linear regression, where relative altitude served as a predictor. Relative altitude is the difference between a grid node (or station) elevation and the average elevation within a radius of 5 km. Secondly, the regression residuals were interpolated by means of inverse distance weighting and subsequently added to the background field.

As part of the European Climate Assessment (ECA) project, Haylock et al. (2008) created daily datasets of maximum and minimum temperatures and precipitation at 0.25° resolution (also known as E-OBS datasets). The datasets were extended by Van den Besselaar et al. (2011) to include daily grids of sea level pressure (SLP). All datasets were produced using a two-step approach, combining an underlying monthly

trend defined by thin plate splines (TPS) interpolation with kriging of daily anomalies. The two gridding steps were adapted to the characteristics of the specific variable. 3D TPS was used for the monthly mean temperature. However, interpolation of monthly mean SLP was done using 2D TPS as it has no elevation dependence. While daily temperature anomalies were interpolated using kriging with external drift to capture elevation effects, simple kriging was applied to daily pressure anomaly.

Evaluations by Hofstra and New (2009) and Kysely and Plavcova (2010) showed a high level of concordance between the E-OBS dataset and regional high-resolution datasets. However, particularly in regions of complex terrain and low station coverage, substantial biases were also detected. This can be explained by the interpolation methods applied to generate the E-OBS datasets, which are tuned to provide, on average, minimum interpolation errors. As a result, however, local heterogeneities cannot be accounted for, and locally varying climate conditions may therefore be hidden. For example, since no suitable secondary information was used, effects on air temperature due to cold air drainage flow or exposure are not adequately represented everywhere in the E-OBS grids (e.g. Kysely and Plavcova 2010; Frei 2014). To capture sub-daily small-scale phenomena insufficiently resolved by the station network, further predictors and innovative methods are required.

Frei (2014) and Hiebl and Frei (2015) did a lot of pioneering work in this area. Frei (2014) created a daily mean temperature dataset for Switzerland, and Hiebl and Frei (2015) a daily minimum and maximum temperature dataset for Austria, both at 1-km² grid resolution. They applied an interpolation method specifically suited to complex terrain, accounting for both non-linear elevation dependence of air temperature and local topographical features. This was achieved by combining regional-scale background fields based on non-linear vertical profiles with local-scale residual fields derived using non-Euclidean distance weighting.

On the hourly time scale, wind speed and direction exhibit considerable horizontal differences, which cannot be solely captured by statistical means. Major difficulties arise due to the wind's vector character, as well as its sensitivity to local topographic features and surface roughness. Numerical weather models provide quite accurate representations of the current wind pattern at the mesoscale (Senkler und Streit 2000). Statistical downscaling of model wind, a relatively recent development, allows wind to be derived at the local scale. De Rooy and Kok (2004), for example, introduced a combined physical/statistical downscaling approach, where the total error between model and observations is decomposed into a small-scale representation mismatch and a large-scale model error.

Thanks to remote sensing, it is possible to retrieve the spatial patterns of some climate variables over extended regions

as well as at high spatial resolution and high sampling rate (Holmes et al. 2009). The Satellite Application Facility on Climate Monitoring (CM SAF) of EUMETSAT provides high-resolution datasets (space $\sim 25 \text{ km}^2$ over Germany, time: below hourly) for cloud cover, global radiation (SIS) and direct radiation (SID) covering most of Europe and Africa from 1983 onwards (Posselt et al. 2013; Krähenmann et al. 2013). Evaluations of daily SIS and SID (Müller et al. 2015) against high-quality in situ observations from the Baseline Surface radiation Network (BSRN; Ohmura et al. 1998) revealed overall high anomaly correlation ($r = 0.95$ for SIS and 0.92 for SID) and biases of $+1.12 \text{ W/m}^2$ for SIS ($\sim 1\%$ of the daily means over the period 1999–2014) and $+0.78 \text{ W/m}^2$ for SID ($\sim 2\%$ of the daily means over the period 1999–2014). Yet, substantial biases were detected in regions of complex terrain mainly caused by cast shadow effects and heterogeneous cloud patterns, and for winter months due to errors resulting from snow coverage.

Surface down-welling longwave (SDL) radiation is mainly determined by temperature, water vapour in the lower atmosphere and the cloud base height (Ohmura 2001). Satellite-based information alone does not provide enough information to retrieve SDL of a sufficiently good quality. The dominant contributor to surface up-welling longwave radiation (SOL) is the surface temperature, which is derived from satellite observations under clear-sky conditions (Karlsson et al. 2013). Following Karlsson et al. 2013, the CM SAF has developed an SDL radiation dataset which combines the monthly mean SDL from ERA-Interim reanalysis with satellite-based cloud cover and high-resolution topographical information. To derive a monthly SOL dataset, CM SAF used SOL radiation data was based on the European Centre for Medium-Range Weather Forecasts' (ECMWF) ERA-Interim reanalysis (Dee et al. 2011), as well as surface emissivity information and high-resolution topographic information (Karlsson et al. 2013). Both datasets are available at 0.25° resolution and cover the period 1982 to 2013.

This paper describes the construction of a 1 km^2 hourly dataset of several surface climate variables covering Germany. The gridding methodology applied depends on the climate variable and utilizes station-based and satellite-derived observations as well as data from a high-resolution regional climate model. The gridded dataset comprises 12 climate variables including air and dew point temperature, cloud cover, wind speed and direction, global and direct short-wave radiation, down- and up-welling longwave radiation, and sea level pressure and the secondary variables relative humidity and water vapour pressure.

The dataset was primarily generated to update Germany's test reference years (TRY), a dataset for technical climatology, but will also address a wider audience requiring climate data at a very high spatial and temporal resolution. The TRY is an artificial set of hourly data of 365-day length and consists of

real measurements covering several parameters such as air temperature, surface radiation and wind speed. The TRY is made up of a number of appropriate sections (between ten days and a month long) within the period 1995 to 2012, with air temperature being the leading parameter (annual cycle close to the climatological one and natural distribution of its higher and lower values on a single day). TRY datasets are mainly designed for application in the field of heating, cooling and air conditioning systems. TRY also serves as input data for thermal building simulations, yielding information on the energy consumption of heating and cooling systems.

The TRY data were first developed in 1986 as part of a research project initiated by the then Federal Ministry of Research and Technology and led by the Institute for Geophysical Sciences of the Free University of Berlin (Blümel et al. 1986). The first TRY datasets to cover Germany as a whole were published in 2004 (Christoffer et al. 2004) and updated between 2008 and 2011 (Spekat et al. 2011). At this time, the former period (1961 to 1990) was updated to include the period between 1993 and 2007, and a city climate module implemented to estimate the urban heat island (UHI) effect. In view of Germany's huge size, the TRY datasets were based on the division of Germany into 15 climate regions with one representative station for each region. However, since this meant that the current TRY data were not equally representative everywhere, in 2013, the Federal Institute for Research on Building, Urban Affairs and Spatial Development (BBSR) commissioned new local TRY datasets for every square kilometre of Germany as a reference guide for building construction on a local scale (Krähenmann et al. 2015). Both, the TRY data and the dataset from which the TRY data are derived will be publicly available from the Deutscher Wetterdienst.

The structure of the paper is as follows. In Sect. 2, the station and satellite observations, the regional climate model and the digital elevation model are briefly described. Section 3 introduces the variable-dependent methodologies used to derive the continuous fields. In Sect. 4, interpolation errors are assessed and examples are shown to illustrate some of the characteristics of the gridded dataset. Section 5 summarizes the paper and some conclusions are drawn.

2 Data

The dataset presented comprises 12 meteorological variables with hourly resolution, including air and dew point temperature, relative humidity, vapour pressure, sea level pressure, cloud cover, wind speed and direction and the surface radiation components global and direct shortwave, down- and up-welling longwave.

The main source of data used to construct the gridded datasets was synoptical and climate station data. In the cases

of low station coverage or high spatial variability of a specific climate variable, the integration of predictor data can greatly improve the data grids. In this connection, elevation (e.g. air temperature) and satellite-derived data (e.g. cloud cover and solar radiation) were considered useful predictors.

Data from a high-resolution regional climate model (COSMO-CLM; Böhm et al. 2006) were used to support the gridding of wind speed and direction and the two longwave radiation components (Table 1). The model has proven to perform well over Europe in comparison with other RCMs (e.g. Berg 2013; Hermans et al. 2012; Vautard et al. 2013). The model simulation accounts for overflow and channelling effects in complex terrain and regional wind patterns in consideration of physical laws. Longwave radiation is only measured at a few German stations. The grids of the longwave radiation components were therefore generated by combining modelled longwave radiation data with satellite-derived cloud cover.

2.1 Station data

Synoptical and climate station data (except radiation) used to construct the gridded datasets were extracted from the DWD relational database management system MIRAKEL. Data obtained from automated synoptical stations have hourly time resolution, while observations from manual climate stations are provided three times per day. The increase in the number of stations available for the interpolation process with missing data of less than 30% is given in Fig. Fig. 1. The network density depends on the climate variable, with the highest station number for temperature and the lowest for longwave radiation (Fig. Fig. 2). Measurement precision differs among the variables and is generally lower for climate stations (see Sect. 2.1.2).

For air and dew point temperature, station data from neighbouring countries was also used to heighten precision close to the borders. Figure Fig. 2a provides an overview of

the stations with less than 30% missing data (~250 synop stations). Climate stations (~600; not shown) provide observations only three times per day, and they were solely used to derive the vertical lapse-rate of air and dew point temperature (see Sect. 3.1).

To improve temporal and spatial consistency of the climate datasets, relative humidity and vapour pressure were derived from the previously interpolated grids of air temperature, dew point temperature and absolute air pressure (Frick et al. 2014). While synop weather stations provide dew point temperature, for the climate stations, it has to be calculated from air temperature and relative humidity using the Magnus formula (Magnus 1844). For dew point temperature, the station coverage is similar to that of air temperature (Fig. Fig. 2b).

Wind speed is measured at heights above the surface of generally between 2 and 20 m with the majority of measurements taken at 10 m. However, as the wind field represents speed at a height of 10 m, and as the measurement height has a considerable impact on wind speed, only measurements of 10 ± 2 m in height were used. Additionally, measurement precision was considerably lower for climate stations, and these have been discarded as a consequence. All stations fulfilling the requirements and with less than 30% missing data are depicted in Fig. Fig. 2c (~150 stations).

The gridding of air pressure is based on the sea level pressure which varies more continuously (SLP). Apart from few exceptions, the stations provide both absolute and sea level pressure. For the remaining stations, SLP was calculated using the formula employed at the Deutscher Wetterdienst (DWD 2008):

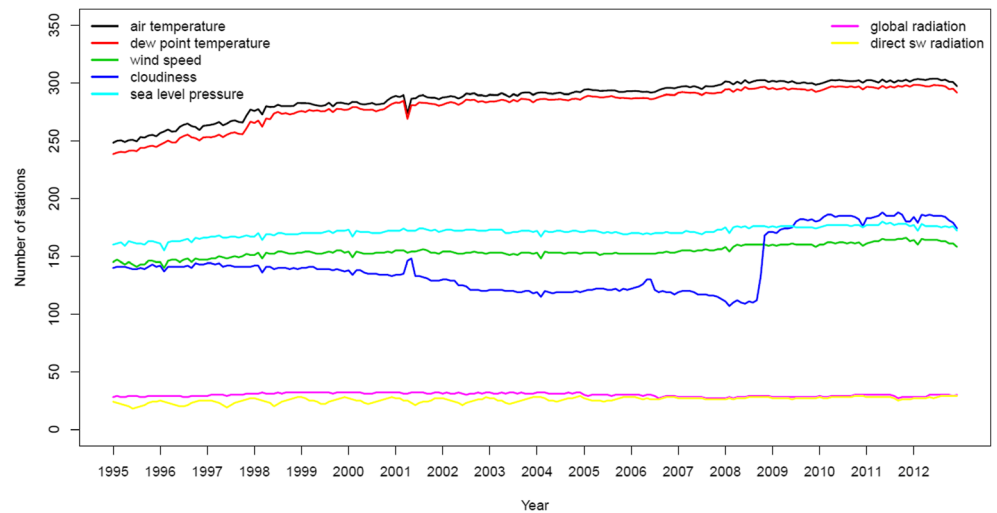
$$p_0 = p(h) e^{\frac{g_0 z}{R(T + C_h * E + \frac{g_0 z}{2})}} \quad (2.1)$$

with $p(h)$ as the absolute air pressure (hPa) and p_0 as the air pressure reduced to sea level, g_0 as the gravitational acceleration ($9.80665 \text{ m}^2/\text{s}^2$), R as the gas constant of dry air

Table 1 Data sources used for the gridding procedure

Climate variable	Station data	Satellite data	RCM data
Air temperature (°C)	X		
Dew point temperature (°C)	X		
Relative humidity (%)	X		
Vapour pressure (g/kg)	X		
10-m wind speed (m/s)	X		X
10-m wind direction (°)	X		X
Sea level pressure (hPa)	X		
Global radiation (W/m^2)	X	X	
Direct solar radiation (W/m^2)	X	X	
Down-welling longwave radiation (W/m^2)		X	X
Up-welling longwave radiation (W/m^2)		X	X
Cloud cover (1/8)	X	X	

Fig. 1 Number of stations with less than 30% missing data for each month. For SLP, only stations up to 600 m were counted



($287.05 \text{ m}^2/\text{s}^2/\text{K}$), z as the elevation (m), T as the 2-m temperature (K), E as the water vapour pressure (hPa), Ch as the additional value to account for the vertical vapour pressure gradient (K/hPa; here set to one; WMO 1959) and a as the vertical temperature gradient: $0.65 \text{ K}/100 \text{ m}$.

The DWD formula (Eq. 2.1) becomes more uncertain as altitudes increase. Thus, to minimise uncertainty, only synop stations (regardless whether they provide absolute or sea level pressure) up to 600-m elevation were considered for the gridding (~ 160 ; see Fig. Fig. 2e).

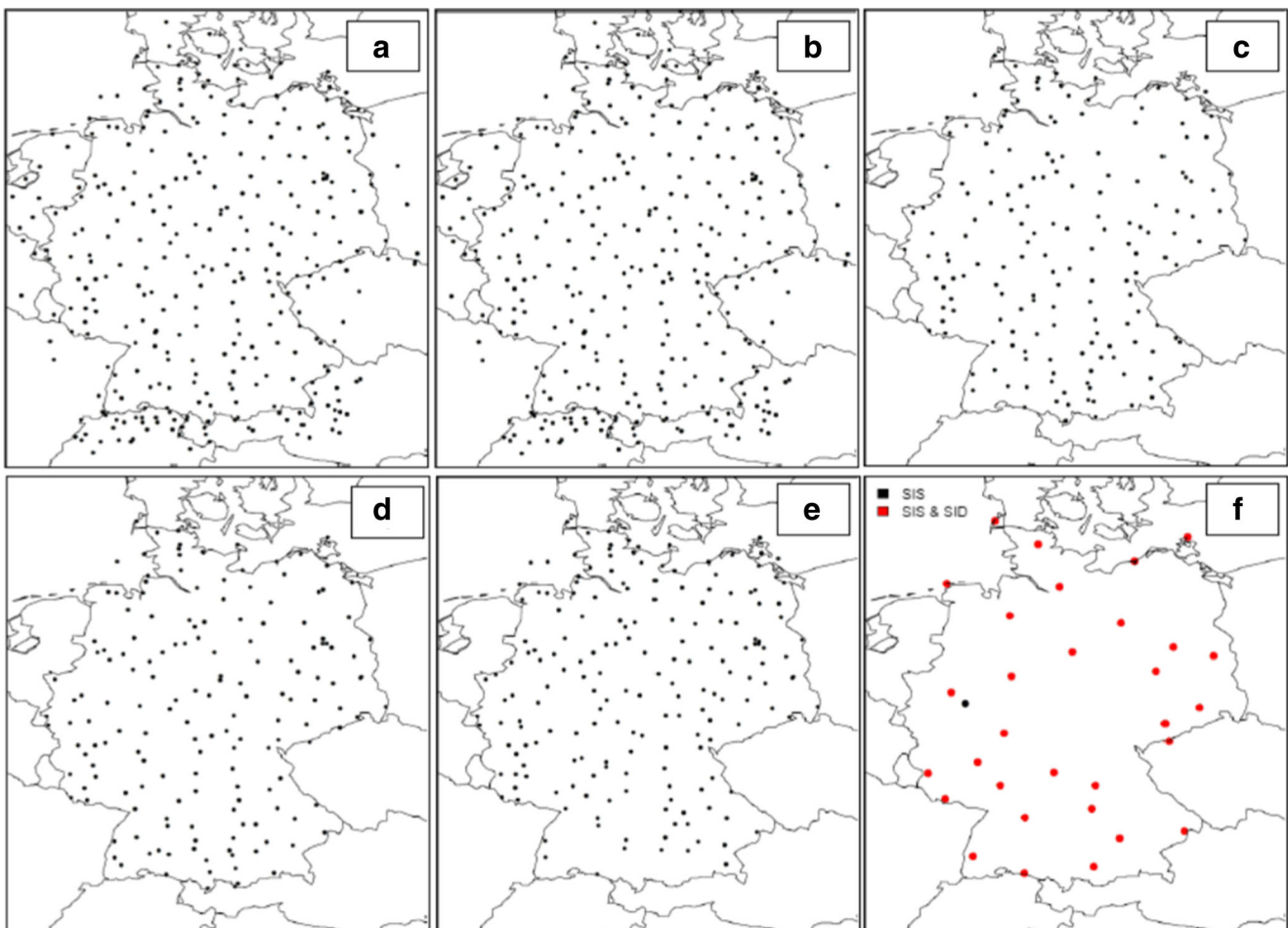


Fig. 2 Location of observing stations used for gridding with, on average, less than 30% missing data: **a** air temperature, **b** dew point temperature, **c** wind speed, **d** cloud cover, **e** sea level pressure and **f** global and direct radiation

About 150 DWD stations provide observations of cloud cover with less than 30% missing data (see Figs. Fig. 1 and Fig. 2d). Cloud cover is considerably affected by topographic barriers or strong winds and may vary considerably in time and space. Cloud patterns are often geographically constrained and thus be insufficiently captured by ground-stations. For this reason, satellite-derived cloud data was used to grid cloud cover alongside ground-based observations (see Sect. 3.3).

Within the DWD network, both global and diffuse radiations are observed at about 30 manned stations (Fig. Fig. 2f) using Kipp and Zonen pyranometers (Kipp and Zonen 2004). The pyranometer is a high-end instrument (ISO 9060 classification: secondary standard referring to high quality) with a spectral coverage of 0.3–2.8 μm .

Eleven sites are equipped with Kipp and Zonen pyrgeometer to measure downward atmospheric longwave radiation (not shown; Kipp and Zonen 2004). Daytime measurements showed considerable uncertainty with differences of up to 20 W/m^2 (e.g. Becker and Behrens 2012), mainly due to interferences from shortwave radiation with longwave measurements. Hence, ground-based observations were solely used for validation purposes. For the gridding of the longwave radiation components, we combined model data with satellite-derived cloud fraction (see Sect. 3.5).

2.1.1 Data quality

The time series taken from the MIRAKEL database underwent several quality tests (Jansen and Sedlatschek 2001) to identify and remove suspicious values. Primarily, a series of formal tests was performed, including checks for internal consistency (e.g. dew point temperature cannot be higher than air temperature), parameter-specific (temperatures not below -50 or above 50°C) and climatological (site specific) thresholds. In addition, the time series of synop stations were tested for temporal consistency following Vogelsang (1993). Climate stations were not tested for temporal consistency, because they provide only three observations per day (for large time differences between two measurements, also large value differences become feasible).

Homogeneity of the station data was assessed using the Standard Normal Homogeneity Test (SNHT; Alexandersson and Moberg 1997). For this reason, the station records were divided into reference series (almost) without inhomogeneities and candidate series. For each candidate series, the three best correlated reference series were selected and weighted-averaged according to correlation. Potential reference series were chosen using a graphical method (Rhoades and Salinger 1993), which uses cumulative differences of pairs of de-seasonalized time series.

Radiation data are routinely checked at the DWD meteorological observatory Lindenberg. Basic quality checks

include astronomical and empirical considerations, some interdependencies such as the relation between total and diffuse flux, and cross checking with sunshine duration (Becker and Behrens 2012). In addition, a calibration cycle of 30 months is implemented for clear sky cases, observations are compared with time series derived from radiative transfer simulations. This allows for detection of sensor degradation, inappropriate calibration or configuration and local disturbances.

2.2 Satellite data

The datasets of global radiation (SIS), direct radiation (SID) and effective cloud albedo (cloud albedo (CAL), cloud fractional cover (CFC)) are based on data obtained from EUMETSAT's geostationary Meteosat satellites of the First and Second Generation (MFG and MSG). The Meteosat Visible and InfraRed Imager (MVIRI) instruments on board the MFG satellites scan the earth's disc with a frequency of 30-min intervals and incorporate three channels within the visible and near infrared spectrum. The broadband visible channel (0.45 to 1 μm) is used for the retrieval of CAL, SIS and SID and has a horizontal resolution of 2.5 km at the earth's surface point directly below the satellite (nadir). The Spinning Enhanced Visible and Infrared Imager (SEVIRI) instruments on board the MSG satellites have an observation frequency of 15 min in 12 spectral channels. Two narrow-band visible channels are centred at 0.6 and 0.8 μm , and have a slightly lower resolution than the MVIRI sensor (3 km at nadir).

Posselt et al. (2013) and Müller et al. (2015) combined the two visible channels of SEVIRI using a linear combination proposed by Cros et al. (2006) and applied a modified version of the Heliosat method (Beyer et al. 1996) to produce continuous datasets of CAL, SIS and SID from 1983 onwards that meet climate quality requirements. The effective CAL determined using the modified Heliosat method is combined with clear-sky radiances estimated by the clear-sky model Mesoscale Atmospheric Global Irradiance Code (MAGIC; Müller et al. 2015) to calculate SIS and SID. An integrated self-calibration parameter minimizes the impacts of satellite changes and artificial trends due to degradation of satellite instruments (Müller et al. 2011).

Effective CAL takes values between 0 (cloudless) and 1 (overcast). The deviation of the current reflection from that for cloudless conditions is a measure of the current cloud fraction. However, CAL is based on observations in the visible spectrum and is therefore only available by day. Cloud cover at night could not be observed before MSG was launched in 2005. Near infrared radiances captured by the SEVIRI sensors are used to derive a cloud mask (CFC) applying the NWC SAF/MSG 2010 retrieval algorithm. CFC contains four categories: overcast, cloudless, cloud contaminated and grid points defined as unclear.

For consistency reasons, daytime cloud cover grids have in all cases been produced combining CAL with station

observations. Nocturnal cloud cover could not be directly gridded before 2005 because CFC data were not available. To overcome this issue, typical cloud patterns were used as predictor fields for linear regression against in situ observations (further details in Sect. 3.3). These patterns were determined applying a principal component analysis (PCA) to 6-h averages of satellite-derived nocturnal CFC data from the period 2006 to 2012.

2.3 RCM data

The three-dimensional non-hydrostatic regional climate model COSMO-CLM (CCLM; Böhm et al. 2006) is the climate version of the operational weather forecast model COSMO (developed by the “Consortium for Small-scale Modelling”; Steppeler et al. 2003; Baldauf et al. 2011) used by the German and other Meteorological Services. The climate version is maintained and further developed by the international Climate Limited-area Modelling (CLM) Community. The model prognostically solves compressible equations for wind, temperature, pressure, specific humidity, cloud water, cloud ice content, rain, snow and optionally graupel.

The equations are solved on an Arakawa-C grid (Arakawa and Lamb 1977) defined on a rotated geographical coordinate system. In the vertical, a hybrid coordinate is used. Close to the surface, the numerical layers are terrain-following, flattening out towards the top level of the model. The model physics contains a cloud microphysics scheme (Doms et al. 2011) with prognostic precipitation and four hydrometeor species (cloud droplets, raindrops, cloud ice and snowflakes), a mass flux scheme for convection (Tiedtke 1989) and a delta-two-stream radiation scheme (Ritter and Geleyn 1992). In the standard CCLM version, land surface processes are parameterized by the soil-surface module TERRA_ML (Doms et al. 2011), constituting the lower boundary conditions to the atmospheric model by the provision of energy and water fluxes at the surface. Detailed descriptions of the dynamics, numerical methods and physical parameterizations in the model can be found in the model documentations (Doms et al. 2011; <http://www.cosmo-model.org>).

The simulations are forced by the ERA-Interim reanalysis (Dee et al. 2011) of the European Centre for Medium-Range Weather Forecasts (ECMWF). In a first nesting step, these are downscaled to a grid of 0.11° in the evaluation runs for Euro-CORDEX (Kotlarski et al. 2014). In a second step, these simulations were used to generate the 0.025° (~ 2.8 km) grid. Both nesting steps were performed using CCLM version 4.8.17. For the 0.11° grid, the model domain matches the CORDEX Europe domain with an additional sponge zone of 10 grid points at each side, in which boundary data are impressed on the model. The horizontal domain has a size of 450 grid-points from West to East and 438 grid-points from South to North, including the sponge zone. The high-resolution simulation

(grid spacing 2.8 km) covers Germany and surrounding areas, and the number of grid points is 420×461 . The vertical coordinate has 40 levels for the CORDEX run and 51 levels for the final grid, respectively, with the upper most level at about 22 km above sea level, in both simulations. The other settings of the model parameters are similar for both nesting steps. The major difference in the physical parameterization settings is that for the high-resolution run, the parameterization for deep convection is switched off. A Runge-Kutta integration scheme has been used with time steps of 100 s for the first nesting step and 25 s for the second nesting step. The simulation was carried out for the period 1994 to 2012.

2.4 Predictor data

Elevation data was obtained from the aggregated Shuttle Radar Topography Mission (SRTM) with grid spacing of three arc seconds (Jarvis et al. 2008). The dataset is based on a digital elevation model at one arc second (~ 30 m) with an absolute height error of less than 16 m and a relative positioning error of less than 10 m (Farr et al. 2007). The elevation dataset was required to derive non-Euclidean distances and a special coastal distance measure for temperature interpolation (more details in Sect. 3.1) and relative altitude for wind speed (see Walter et al. 2006). Elevation data were also used to determine land cells.

The latest version of the Coordination of Information on the Environment (CORINE) land cover (CLC; Keil et al. 2011) dataset for Germany was applied to derive surface emissivity (affects up-welling longwave radiation; see Wilber et al. 1999), roughness length (affects wind speed; see Koßmann and Namyslo 2007) and urban heat island intensity (UHI; affects air temperature). The CLC dataset comprises 44 classes and has a resolution of 100 m.

3 Gridding procedure

In order to produce gridded datasets of meteorological variables, values at locations where no observing stations are available need to be estimated on the basis of information provided by surrounding stations. In cases where neighbouring stations are rare, it is possible to improve the estimates of specific variables by using “hybrid” interpolation techniques, i.e. interpolation techniques which combine two different concepts (Hengl et al. 2007). A trend model (linear or non-linear) describing the relation between a specific variable (e.g. air temperature) and secondary data (e.g. altitude) is used to define a background field. The residuals (difference between background field and observed values) are then interpolated using methods such as inverse distance weighting (IDW), Kriging (Journel and Huijbregts 1978) or Thin Plate Splines (TPS; Hutchinson 1998), depending on the variable.

Alternatively, if the station density is particularly low (e.g. radiation data) or the level of variance explained by available secondary data is low, satellite-derived or model-based datasets were also used to derive the background field. However, residual interpolation was not performed for longwave radiation because the station density is too low.

The dataset presented uses the Lambert conformal conical (LCC) projection for Europe based on the European Terrestrial Reference System 1989 (ETRS89) with resolution 1 km², covering German land cells only. The ETRS89-LCC Europe projection with standard parallels 65° N and 53° N and reference coordinates 10° E/52° N constitutes an approximately equidistant grid.

The following section briefly describes the various interpolation procedures used for the gridding of the climate variables. The overall gridding procedure is illustrated by a flow-chart in Fig. 3.

3.1 Air temperature and dew point temperature

In general, the interpolation methods applied to air temperature and dew point temperature are similar. To account for the complex and highly variable thermal distributions caused by maritime influences or by mountains, a recently published methodology (Frei 2014; Hiebl and Frei 2015) that combines nonlinear temperature profiles with non-Euclidean spatial representativeness of observations was adapted to German conditions.

The background field is derived from a large-scale non-linear vertical temperature profile fitted to station data that

varies evenly across Germany and allows inversion layers of various depth and magnitude (Frei 2014; Hiebl and Frei 2015). Vertical profiles are derived separately for eight gradually overlapping sub-regions over Germany (Fig. Fig. 4). Valley stations prone to local-scale cold-pools (identified from average diurnal temperature ranges) are not considered in the estimation of the vertical profile.

The residual field is derived through distance-weighted interpolation of the station deviations to the background field. The weighting scheme is based on a set of predefined distance fields derived from a non-Euclidean distance metric that accounts for the modification of the horizontal exchange of air-masses due to topographic barriers (Frei 2014; Hiebl and Frei 2015). λ is a dimensionless layering coefficient which describes the additional penalty in the horizontal distance as a function of elevation changes (meters per meter). If λ equals 0 the distance becomes Euclidean, a larger λ results in stronger vertical layering of the residuals. The coefficient λ varies in time and is determined using cross-validation.

This interpolation method was originally set up for local conditions across Switzerland and daily mean temperature (Frei 2014). The hourly resolution required for the creation of the TRY data imposes a number of new challenges for the method, and consequently, careful configuration and several methodological modifications were needed. In the following, the configurations and modifications are briefly described:

- The background field is based on vertical profiles derived for subjectively defined sub-regions that are then merged by linear weighting across an overlapping area. The vast area of Germany and its climatic diversity require a more

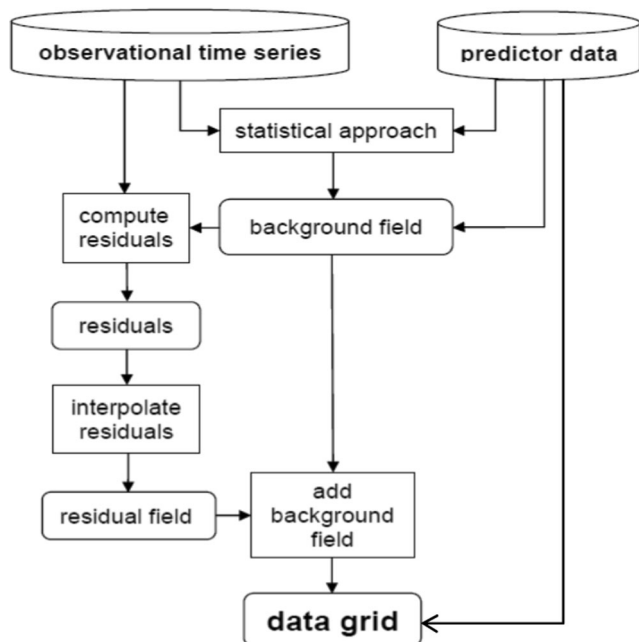


Fig. 3 Procedure to derive the gridded dataset from station data and predictors

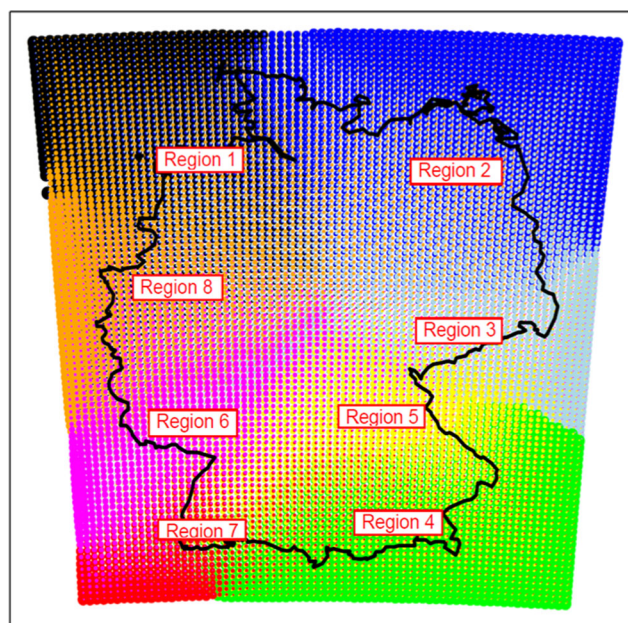


Fig. 4 The sub-regions used for the vertical temperature profiles are mapped in colour. The point size represents the region weight

refined regionalization of the vertical temperature dependence in the background field. In total, eight sub-regions were defined accounting for weather barriers (e.g. Black Forest, Harz, etc.), distance to the sea and the Alpine foothills. This reduces disturbance of the vertical temperature gradient by horizontal gradients. The eight-part division clearly improves the result when there are strong horizontal contrasts, e.g. due to a frontal passage.

- Definition of the generalized distance fields across vast areas and high number of stations results in high computational costs (distance fields calculated prior to interpolation process). Frei (2014) derived the distance fields for every station across the whole of Switzerland. To reduce computational costs, the area for which the distance is calculated was defined according to the station type. For synop and international stations from neighbouring countries, the distance fields were calculated over $400 \times 400 \text{ km}^2$. For mountain stations, the spatial range considered was $600 \times 600 \text{ km}^2$, as stations are generally situated at mountain peaks and, therefore, certain height levels (e.g. between low land and mountain peaks) are insufficiently represented (e.g. at large distances). Because climate stations only provide observations three times per day, they were not used within the residual interpolation process. This adaptation does not constrain the number of stations available for a grid point. Residual weighting was done using the five closest stations.
- Due to the high spatial and temporal resolution of the dataset, it is important to consider the urban heat island (UHI). Prior to the interpolation process, the station time series were UHI adjusted (e.g. subtraction of the estimated UHI effect). The current UHI intensity was calculated according to Wienert et al. (2013), based on time of the day and season, current weather conditions (average cloud cover and wind speed in the last 24 h) and the size of an agglomeration. In the original approach by Wienert et al. (2013), the maximal possible UHI intensity was related to city population. In the present study, we defined the maximum UHI intensity according to building structure and density within a radius of 3 km around a station (derived from CLC land use data; Keil et al. 2011). This is discussed in more detail in the Appendix section. In addition, the generalized distance field was modified using an UHI mask, with a distance penalty depending on the UHI intensity difference between a station and the target grid points (distance in km increases quadratic per $^{\circ}\text{C}$). This prevents the UHI intensity from mixing with topographic effects. Following up on the interpolation, the current UHI intensity was added to the temperature map, depending on building structure, time of the day, season and the current weather situation.
- A cloud cover mask was defined to reduce disturbance of cloud effects with topographical effects. Thereby, the difference in cloud cover (octa) between every station and a

target grid point was converted into distance (distance in km increases quadratic per octa). Cloud cover strongly affects the temperature pattern on short time scales. During the night, clouds reduce the thermal emission and thereby increase the air temperature locally. During the day, an increase in cloud cover reduces the solar radiation reaching the ground and hence decreases the air temperature. The spatial expansion of fog or convective clouds can change quickly.

- The maritime influence on the temperature distribution is considered in the residual interpolation by defining a hypothetical “coastal mountain”. This means that a virtual elevation was added to the digital elevation model depending on the distance to the coastline. The elevation surcharge is highest close to the coast, reaches 500 m at a distance of 100 km from the coast and then remains constant at 500 m. This affects the predefined distance fields derived from the non-Euclidean distance metric, increasing the distance from any grid point off the coast to the coastline.
- Complete daily cycles are necessary for the TRY selection. To improve temporal consistency of the high-resolution temperature maps, interpolation was performed in three steps. Step 1 involved the estimation of the background field seven times per day (the chosen number constitutes a compromise between short time steps and computational costs). In step 2, hourly background fields were calculated by weighting the three temporally closest background fields (weights are linearly proportional to one divided by the temporal difference, if the time difference is zero the weight is set to one). The third step was an hourly residual interpolation. Moreover, a simple gap-filling procedure was applied to provide complete time series on a daily basis (only for single missing hours). The series were divided into reference series without missing data (on that day) and candidate series. For each candidate series, the three highest correlated reference series were given a weighted average (weights are linearly proportional to one divided by the correlation coefficients). Next, the hourly difference between candidate and reference series was filled using a 3-h running mean. In order to fill the hourly missing data in the candidate series, the value of the respective hour of the smoothed mean differences was added to the hourly value from the reference series.

3.2 Relative humidity and vapour pressure

Both relative humidity and vapour pressure depend on atmospheric moisture content and air temperature. The dew point is the temperature to which humid air must be cooled (while air pressure stays constant) when it

becomes fully saturated. Peixoto and Oort (1996) have shown that dew point temperature and vapour pressure provide equivalent information. Hence, we decided to interpolate both temperature parameters and air pressure first and subsequently to derive the humidity parameters from these.

Relative humidity is in general lower over urban areas (Oke 1987; Kuttler et al. 2007). In situ measurements in cities of the mid-latitudes revealed that the night-time maximum relative humidity shows deficits of more than 15% compared to rural areas (Kuttler et al. 2007). The deficit mainly results from higher urban temperatures (UHI) and lower latent heat flux compared to rural areas. However, during clear and calm summer nights, urban locations can have a higher vapour pressure (but lower relative humidity; Kuttler et al. 2007) than rural areas, particularly in the second half of the night. To our knowledge, there are no empirical formulas available to estimate urban to rural humidity differences in meteorological variables. Therefore, this effect was merely accounted for by interpolating air and dew point temperature.

Relative humidity rh is calculated from 2m air temperature T and dew point T_d using:

$$rh = 100 \frac{e(T_d)}{e(T)} \quad (3.1)$$

Water vapour content wv [g/kg] can be derived from dew point T_d and air pressure p_b :

$$wv = \frac{621,98 \cdot 1,0047 \cdot e(T_d)}{p_b - 1,0047 \cdot e(T_d)} \quad (3.2)$$

Saturation vapour pressure over super-cooled water e_w is slightly higher than over ice e_i . It is calculated as follows:

$$\ln e_w(T) = -6096,9385 \cdot T^{-1} + 16,635794 - 2,711193 \cdot 10^{-2} \cdot T + 1,673952 \cdot 10^{-5} \cdot T^2 + 2,433502 \cdot \ln T \quad (3.3)$$

$$\ln e_i(T) = -6024,5282 \cdot T^{-1} + 24,7219 - 1,01613868 \cdot 10^{-2} \cdot T - 1,3198825 \cdot 10^{-5} \cdot T^2 - 0,49382577 \cdot \ln T \quad (3.4)$$

with T being the 2 m air temperature or dew point (K), g_0 the gravitational acceleration ($9.80665 \text{ m}^2/\text{s}^2$), e the vapour pressure over water (e_w) or ice (e_i) (hPa) and p_b the pressure in station height (hPa).

Here, saturation vapour pressure was solely derived using Eq. 3.3, as the available data do not provide information on whether dew point temperature was obtained over water or ice. In general, the resulting error is small. It may only become considerable for temperatures below -10°C .

3.3 Cloud cover

Cloud cover can vary strongly in time and space. Moreover, orographic blocking and strong winds produce complex spatial cloud structures. Variability of cloud patterns affected by topography cannot be adequately captured by surface stations. Satellite-derived cloud cover provides comprehensive information on the current cloud pattern in high spatial ($\sim 25 \text{ km}^2$) and temporal (30 min) resolution. Cloud albedo (CAL), which is available from 1983 onwards, is derived from radiances in the visible spectrum and hence only available during daytime. The SEVIRI instrument on the geostationary satellite only started providing information in the near infrared spectrum in 2005, making cloud fraction (CFC) detection possible by day or night. However, all satellite-derived cloud cover tends to be underestimated in mornings and evenings (Dürr et al. 2013) and is therefore merged with in situ observations.

For consistency reasons, cloud cover was derived from CAL whenever it was available. CAL contains values range from 0 (cloudless) to 1 (overcast sky), and thus ground-based data were transformed to match that range. Hourly CAL data were weighted averaged from the three temporally closest half-hourly values. Hourly CAL served as background field, whereas in situ observations were treated as the truth. Since, ground-based data are valid for a circle of about 30-km radius ($\sim 2800 \text{ km}^2$, in flat areas) and CAL data for an area of about 25 km^2 , residuals (e.g. fraction of satellite-derived to ground-based observations, to account for the lower and upper bounds of cloud cover) were computed from averages of the nearest 200 grid points to every station. Residual interpolation was done by IDW interpolation, using the 12 closest stations. Multiplication of background field and interpolated residuals yielded the cloud cover grids.

To derive nocturnal cloud cover grids before 2005, the dominating cloud cover patterns derived from principal components analysis (PCA) served as predictors. These patterns are related to often re-occurring weather conditions and contain local features. Typical patterns were derived for every calendar month from six-hourly averages of all available CFC images in the period 2006–2012. Interpolation consists of two steps, including multiple linear regression and residual interpolation using IDW. The first 13 PC loadings ($\sim 80\%$ explained variance; example provided by Fig. Fig. 5), longitude, latitude and elevation served as predictors for the regression. Residual interpolation used the 12 closest stations for weighting. As for CAL interpolation, residuals were computed from averages of the nearest 200 grid points to every station.

3.4 Shortwave radiation components

Satellite-based observations of shortwave radiation components are available every 30 min (Posselt et al. 2013). The

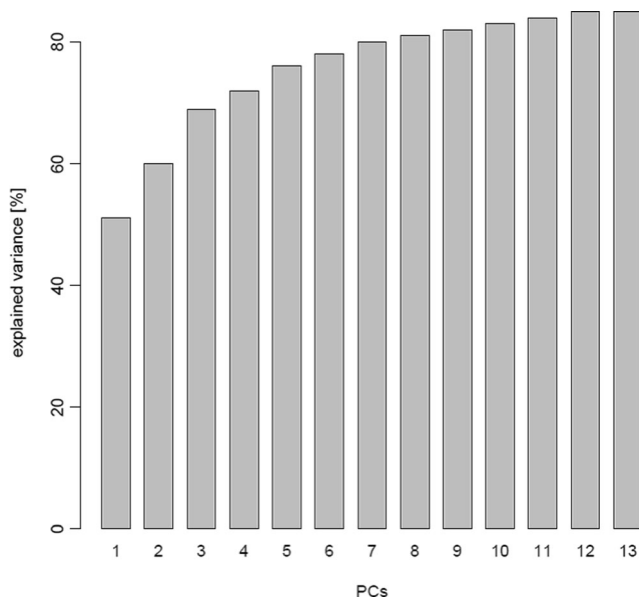


Fig. 5 Cumulative explained variances (%) for the 13 first PC loadings for July 1–6 MEZ

TRY dataset requires hourly means, however. Hence, for every hour HH, the three temporally closest satellite images to the timespan HH–60 min until HH were averaged (weighted according to the time difference of the satellite images to HH–30 min). The resulting hourly means contain a small error due to the nonlinearity of the daily radiation cycle. We tackled this issue by applying a correction factor which corresponds to the ratio of the true extra-terrestrial radiation and the extra-terrestrial radiation calculated from the times of the three satellite images for the hour HH.

To derive the all-sky surface irradiance for global radiation (SIS) or direct shortwave radiation (SID) from satellite data, the clear-sky radiation is linked to a cloud index, which acts as a proxy for cloud transmittance (Beyer et al. 1996; Posselt et al. 2013). The underlying cloud index which is needed for calculating short wave radiation is derived from the brightness difference between the current situation and a reference value. Cloud extinction is empirically derived from the clear-sky irradiance whenever the cloud index indicates presence of clouds (Cano et al. 1986). The separation of direct and diffuse radiation components can be subject to errors, particularly for thick clouds. Uncertainties in the prescribed humidity of the atmosphere (derived from NWP-models) and aerosols (climatology) also lead to errors in satellite-derived radiation data, especially under clear-sky conditions (Müller et al. 2015).

A comparison between satellite-based and ground-based data revealed specific errors depending on location, season and presence of snow. It is particularly difficult to distinguish snow from clouds as both are good reflectors of shortwave radiation. Radiances obtained at 32 ground-based pyranometer stations were used to correct the bias of the satellite-derived shortwave radiances (SIS and SID). Surface stations provide point-wise

observations, satellites, by design, detect spatial mean values ($\sim 25 \text{ km}^2$). This can lead to substantial differences between the two datasets, particularly when cloud cover is variable and averaging periods are short. Hence, the two datasets cannot be directly merged, but resolution-dependent differences average out over longer time periods (e.g. days).

3.4.1 Surface incoming shortwave radiation (SIS)

A correction factor was derived on a daily basis, corresponding to the ratio of the daily totals of satellite-based and surface observations. Before the correction factor could be applied, the hourly satellite data were normalized (e.g. removal of geographical effect) by division through the extra-terrestrial radiation of the specific hour. Subsequently, the correction factors derived station-wise were interpolated by IDW, with a distance measure that accounts for geographical coordinates, elevation and the daily total of satellite-derived SIS. The interpolated correction factors were then applied to the hourly SIS totals assuming a site-specific but constant error throughout the day. To ensure an improvement of the satellite-derived dataset, the correction was only carried out on days for which cross-validation indicated an improvement in terms of both BIAS and MAE.

3.4.2 Surface incoming direct radiation (SID)

The SID to SIS ratio depends on several factors including cloud cover, atmospheric moisture, time of the day and season. This was taken into account when the satellite-based SID dataset was generated (Müller et al. 2015). However, the corrections applied to the SIS dataset in the previous step (Sect. 3.4.1) require an update of the SID dataset, to maintain the coherence between both variables. This was done in a two-step process; the current (weather condition-dependent) SID to SIS ratio was calculated from the original satellite-derived datasets and applied to the corrected SIS dataset, followed by a residual interpolation.

To ensure a sufficiently large sample size, while also accounting for influences specific to time of day, season and current weather conditions, the SID to SIS ratio was derived from a moving window of 11 days (current day ± 5 days). Since the SID to SIS ratio strongly depends on atmospheric moisture and solar elevation, it was individually determined for every hour and in eight overlapping regions throughout Germany (Fig. Fig. 4) and also applied individually to the hourly SIS totals.

Because resolution-dependent differences average out over longer time periods, the interpolation process was carried out on normalized residuals (e.g. after removal of the geographical effect) of daily SID totals. Multiple linear regression was used for interpolation, with geographical coordinates, elevation and the daily total of the corrected SIS dataset serving as

predictors. The corrected daily SID dataset was determined by adding the residual field to the updated hourly SID total (yields the updated daily SID total). The hourly SID fields were corrected by multiplying the updated hourly SID fields with the ratio of the corrected daily SID total to the updated daily SID total.

3.5 Longwave radiation components

Only a few German stations routinely observe surface upwelling (SOL) and surface down-welling (SDL) longwave radiation components (~4 to ~20 μm). To derive the gridded datasets of the longwave radiation components, we therefore used a combination of reanalysis data and satellite-derived cloud fraction.

3.5.1 Surface down-welling longwave radiation (SDL)

To generate SDL fields, an algorithm proposed by Karlsson et al. (2013) was used. The algorithm applies a cloud-dependent radiative forcing (all sky minus clear sky SDL) derived from model data and satellite-derived cloud cover. Here, the radiative forcing was calculated from the down-scaled reanalysis data provided by the regional climate model COSMO-CLM (CCLM). An evaluation study performed by Will and Woldt (2009) showed overall good agreement between satellite-derived and modelled (CCLM) cloud properties, water vapour content and surface longwave radiation components.

The model-based cloud correction factor CCF^{CCLM} was calculated as follows:

$$CCF^{CCLM} = \frac{SDL_{as}^{CCLM} - SDL_{cs}^{CCLM}}{CFC^{CCLM}} \tag{3.5}$$

with SDL_{as}^{CCLM} (SDL_{cs}^{CCLM}) being the modelled all sky (clear sky) down-welling longwave radiation and CFC^{CCLM} the modelled cloud cover.

Since CCLM does not provide SDL_{cs}^{CCLM} , it had to be derived from the air temperature T_a^{CCLM} and the emissivity of the lower atmosphere ϵ_a^{CCLM} :

$$SDL_{cs}^{CCLM} = \epsilon_a^{CCLM} \cdot \delta \cdot T_a^{CCLM^4} \tag{3.6}$$

The emissivity ϵ_a^{CCLM} can be calculated from T_a^{CCLM} and the water vapour content e_a^{CCLM} following Sugita and Brutsaert (1993):

$$\epsilon_a^{CCLM} \cdot 0.714 \cdot \left(\frac{e_a^{CCLM}}{T_a^{CCLM}} \right)^{0.0687} \tag{3.7}$$

To downscale SDL_{as}^{CCLM} to the 1-km² grid CCF^{CCLM} was applied to the gridded cloud cover dataset (CFC^{1km} ; see Sect.

3.3) and added to SDL_{cs}^{CCLM} :

$$SDL_{as}^{1km} = SDL_{cs}^{CCLM} + CCF^{CCLM} \cdot CFC^{1km} \tag{3.8}$$

To account for the elevation effect on SDL_{as} (T_a decreases with elevation), a surcharge of 2.8 W/m² per 100 m (Wild et al. 1995) was added to the previously derived SDL_{as} dataset, which depends on the elevation difference between the CCLM grid and the 1 km² grid.

3.5.2 Surface up-welling longwave radiation (SOL)

SOL_{as} is mainly determined by the surface temperature T_{srf} and the surface emissivity ϵ_{srf} :

$$SOL_{as} = \epsilon_{srf} \cdot \sigma \cdot T_{srf}^4 + (1 - \epsilon_{srf}) \cdot SDL_{as} \tag{3.9}$$

Here, SOL_{as}^{1km} is derived using an approach by Karlsson et al. (2013). In a first step T_{srf}^{CCLM} is calculated using:

$$T_{srf}^{CCLM} = \sqrt[4]{\frac{SOL_{as}^{CCLM}}{\epsilon_{srf}^{CCLM} \cdot \sigma}} \tag{3.10}$$

According to Wilber et al. (1999) the surface emissivity ϵ_{srf}^{1km} was assigned to land use classes of the CORINE dataset (Keil et al. 2011). T_{srf}^{CCLM} was then calculated applying Eq. 3.10 to SOL_{as}^{CCLM} and to aggregated surface emissivity ϵ_{srf}^{CCLM} (to match the CCLM resolution).

To downscale T_{srf}^{CCLM} to the 1-km² grid, a dry adiabatic temperature gradient of -9.81°C per km was assumed:

$$\Delta T_{srf}^{1km} = \Delta z \cdot \Delta T, \tag{3.11}$$

with Δz being the elevation difference between the CCLM grid and the 1-km² grid. SOL_{as} was transformed to the 1-km² grid using:

$$SOL_{as}^{1km} = \epsilon_{srf}^{1km} \cdot \sigma \cdot \left(T_{srf}^{CCLM} + \Delta T_{srf}^{1km} \right)^4 + (1 - \epsilon_{srf}^{1km}) \cdot SDL_{as}^{1km} \tag{3.12}$$

The second term on the right hand side of Eq. 3.12 accounts for the amount of SDL_{as} reflected by the surface.

3.6 Sea level pressure

The gridding of SLP is based on a two-step interpolation approach which was also used within the E-OBS project (Van den Besselaar et al. 2011). The approach involves two dimensional thin plate splines (TPS) interpolation of daily SLP means, followed by kriging of the hourly deviations from the daily mean. As a result, 2-D TPS (with latitude and longitude as independent variables) generate a background field of evenly varying hourly deviations, which is a prerequisite for

kriging interpolation. Summation of the daily background field and the hourly anomalies yielded the hourly SLP grids.

3.7 Wind components

Station-based wind measurements are only representative in their immediate surroundings. The gridding, particularly on the hourly time scale, must therefore consider horizontal differences, which cannot be solely captured by statistical means. In this respect, COSMO-CLM provides quite accurate representations of the current wind field (Grasselt et al. 2008; Geyer et al. 2015).

The wind fields (speed and direction) were produced applying a multi-step procedure proposed by De Rooy and Kok (2004). The regional climate model COSMO-CLM provided a first guess of the field of hourly wind speed and wind direction of 2.8-km resolution. Station data were used for bias correction of the modelled wind. The 1-km² resolution was reached by transforming the wind speed to the local roughness length using the logarithmic wind profile law (Taylor 1987).

3.7.1 Wind speed

Model wind speed and roughness length are both valid for grid node averages. However, station data provide point-wise information valid for local roughness lengths. Prior to the bias correction, both model and station data therefore have to be made comparable. This was achieved using model wind and local roughness information to estimate 10-m wind speed at the station locations. Besides local roughness length, the anemometer height also influences wind speed. Several empirical formulas (Wieringa 1986) are available to transform the wind speed from any measuring height to 10 m, resulting in further uncertainty. Model wind speed was therefore solely localized at stations with anemometer heights of 10 ± 2 m.

In the present study, a methodology proposed by De Rooy and Kok (2004) was applied, which makes use of the theoretical concept of the internal boundary layer and assumes that a height exists above ground at which wind speed becomes independent from the local roughness length. At a certain height (e.g. the blending height), the average wind profiles above a certain grid node and a station located within that grid node converge to a common wind speed (De Rooy and Kok 2004).

Since the blending height is unknown and subject to changing weather, modelled 140-m wind speed (U_{140}) is used as reference wind speed. To transform the model wind at blending height to 10 m and local roughness, the flux profile relation (Monin and Obukhov 1954) is used:

$$u_{10} = u_{140} \frac{u_*}{\kappa} \left[\ln \left(\frac{140}{10} \right) - \Psi_M \left(\frac{140}{L} \right) + \Psi_M \left(\frac{10}{L} \right) \right] \quad (3.13)$$

U_{10} depends on the friction velocity u_* and the Obukhov length L (Obukhov 1946), Ψ_M is the stability function for momentum (Källén 1996) and κ the Karman constant. The surface theory states that u_* and L are vertically constant and wind speed becomes zero at reference roughness length z_0 . For the transformation from z (here the blending height) to z_0 meters, Eq. (3.13) becomes:

$$u_z = \frac{u_*}{\kappa} \left[\ln \left(\frac{z}{z_0} \right) - \Psi_M \left(\frac{z}{L} \right) + \Psi_M \left(\frac{z_0}{L} \right) \right] \quad (3.14)$$

For neutral conditions ($\Psi_M = 0$) with blending height of 140 m and by rearranging Eqs. (3.13) and (3.14), the local wind speed can be calculated:

$$u_{10,loc} = u_{140,clm} \frac{\ln \left(\frac{10}{z_{0,loc}} \right)}{\ln \left(\frac{140}{z_{0,loc}} \right)} = \text{estimator A} \quad (3.15)$$

Estimator A does not depend on the stability function Ψ_M and produces overestimated/underestimated $u_{10,loc}$ for stable/unstable conditions (De Rooy and Kok 2004). To account for atmospheric stability, the following assumption was made: Transforming model wind speed at 140 m, considering the model roughness length but not the stability function, the estimated u_{10} will deviate from the modelled wind speed at 10 m. This deviation corresponds to the stability correction to be applied when transforming wind speed from 140 to 10 m and is simply added to estimator A:

$$u_{10,loc} = u_{10,clm} + u_{140,clm} \left[\frac{\ln \left(\frac{10}{z_{0,loc}} \right)}{\ln \left(\frac{140}{z_{0,loc}} \right)} - \frac{\ln \left(\frac{10}{z_{0,clm}} \right)}{\ln \left(\frac{140}{z_{0,clm}} \right)} \right] \quad (3.16)$$

Estimation of the roughness length Before the wind transformation could be applied, roughness lengths valid for the model grid, the 1-km² grid and the station locations had to be derived. For every station, aerodynamic roughness lengths were assigned to CORINE land use data (Keil et al. 2011) within a 3-km radius and for eight wind directions, following the topographical maps approach by Koßmann and Namyslo (2007). Wind direction-dependent z_0 values were calculated for 25 distance classes. Subsequently, according to the so-called footprint method, distance weights were calculated using the two-parameter Weibull distribution function (Kljun et al. 2004). The roughness lengths for the model grid (~2.7 × 2.7 km²) and the 1-km² grid amount to the spatial average (e.g. logarithmic averaging) of the assigned roughness length within each grid node (see details in Appendix).

Table 2 RMSE (°C) for hourly temperature and eight climate regions (see Fig. 4)

Region	Jan	Feb	Mar	Apr	May	Jun	Jul	Aug	Sep	Oct	Nov	Dec
1	0.8	0.8	0.8	1.0	1.0	1.0	1.0	1.0	0.9	0.9	0.7	0.8
2	0.8	0.8	0.8	1.0	1.0	1.0	1.0	1.0	0.9	0.9	0.8	0.8
3	0.8	0.0	0.8	1.0	1.0	1.0	1.0	1.0	0.9	0.9	0.8	0.8
4	1.3	1.2	1.2	1.2	1.2	1.1	1.2	1.2	1.1	1.2	1.1	1.2
5	1.1	1.1	1.0	1.1	1.1	1.1	1.1	1.1	1.1	1.1	1.0	1.1
6	0.8	0.8	0.8	1.0	1.0	1.0	1.0	1.0	0.9	0.9	0.8	0.8
7	1.1	1.1	1.1	1.1	1.2	1.1	1.2	1.2	1.1	1.2	1.1	1.1
8	1.0	0.9	0.9	1.0	1.1	1.0	1.0	1.1	1.0	1.0	0.9	0.9

Combination of the physical method with linear regression

Subsequent to the roughness-based transformation of the model wind speed to locally valid values at the station locations, a statistical bias correction was applied. According to De Rooy and Kok (2004), two assumptions were made at this point: (1) The regional climate model describes the overall wind field correctly; (2) the model bias depends on the geographical position, so that Germany was split into four overlapping regions (intersection point at 11° E and 51° N). The bias, which is only known at the station locations, was interpolated using multiple linear regression, where spatial coordinates, relative elevation (elevation of a grid node compared to the average elevation within 5-km radius; see Walter et al. 2006) and distance to the coast served as predictors. Regression coefficients were updated on an hourly basis, using observations of the current hour ± 1 h to increase the sample size and to reduce the impact of observing errors.

3.7.2 Wind direction

The regional climate model COSMO-CLM also provided the background field for wind direction, which was bias-corrected using station data. The wind direction given in degrees cannot be directly interpolated. This issue was tackled by converting wind directions into u - (west-east) and v - (north-south) vector components of the wind. The bias of both vector components was only derived at stations with anemometer heights of

10 ± 2 m and where the difference in relative elevation between the station and the nearest model grid node did not exceed 50 m. Bias interpolation was done applying 3D IDW, with a distance measure that accounts for geographical coordinates and relative elevation. Summation of modelled u - and v - components and interpolated residuals of both components with subsequent back transformation yielded the hourly wind direction grids.

4 Results

The interpolation methods described in the previous section were processed over the entire study period 1995–2012. The final dataset consists of more than 157,000 hourly fields of 12 climate variables. Daily, monthly and annual fields were also derived.

The following section provides a summary based on a statistical evaluation of the procedures used by means of cross-validation (Sect. 4.1). In Sect. 4.2, the consistency in time and between the various climate variables is demonstrated on the basis of a hot summer day with a cold front approaching from the northwest. Section 4.3 describes some application examples such as the quantification of extreme years. In the final sub-section, the derived dataset is applied by way of example to derive perceived temperature (Staiger et al. 2012), illustrated by the Rhine-Main area.

Table 3 RMSE (°C) for diurnal temperature range and eight climate regions

Region	Jan	Feb	Mar	Apr	May	Jun	Jul	Aug	Sep	Oct	Nov	Dec
1	1.0	1.1	1.2	1.5	1.5	1.5	1.4	1.5	1.4	1.3	1.0	1.0
2	1.0	1.1	1.2	1.5	1.5	1.5	1.4	1.5	1.5	1.3	1.0	1.0
3	1.1	1.2	1.2	1.4	1.3	1.4	1.3	1.3	1.4	1.2	1.1	1.0
4	1.6	1.8	1.6	1.9	1.7	1.8	1.6	1.6	1.7	1.7	1.6	1.5
5	1.4	1.6	1.5	1.7	1.6	1.7	1.5	1.5	1.6	1.5	1.5	1.4
6	1.0	1.2	1.2	1.4	1.4	1.4	1.3	1.4	1.4	1.2	1.1	1.0
7	1.5	1.6	1.5	1.9	1.6	2.0	1.5	1.5	1.7	1.6	1.6	1.4
8	1.2	1.4	1.3	1.5	1.5	1.6	1.4	1.4	1.5	1.4	1.3	1.2

Table 4 RMSE (%) for hourly relative humidity and eight climate regions

Region	Jan	Feb	Mar	Apr	May	Jun	Jul	Aug	Sep	Oct	Nov	Dec
1	4.8	5.1	5.6	6.4	6.7	6.3	6.4	6.5	5.7	5.2	4.7	4.6
2	4.8	5.1	5.7	6.5	6.8	6.4	6.5	6.6	5.7	5.2	4.6	4.6
3	5.3	5.5	5.8	6.4	6.7	6.3	6.4	6.5	5.6	5.3	4.9	5.2
4	7.9	7.9	7.8	7.5	7.9	7.4	7.8	7.9	6.9	7.3	7.0	7.5
5	6.9	7.2	6.9	7.1	7.3	7.1	7.3	7.3	6.4	6.5	6.3	6.6
6	5.0	5.4	5.7	6.4	6.6	6.4	6.4	6.5	5.8	5.2	4.9	4.8
7	7.7	8.2	7.7	7.9	8.0	7.8	8.1	8.1	7.1	7.2	7.0	7.0
8	5.9	6.4	6.4	7.0	7.1	6.9	7.0	7.0	6.2	5.8	5.5	5.6

4.1 Statistical Evaluation

This section provides an evaluation of the gridded datasets for eight regions in Germany (Fig. Fig. 4) using leave-one-out cross-validation. Leave-one-out cross-validation (in the following abbreviated as CV) means that each data point is removed and that the observed value is re-estimated separately from the remaining data by means of interpolation (Wackernagel 2003). The square root (RMSE) was then calculated from the prediction errors at the stations and averaged over the complete time period 1995–2012 (but separately for each calendar month and region).

Tables 2, 3, 4, 5, 6, 7, 8, 9, 10 and 11 depict the results for each evaluation region and variable. The highest relative prediction errors were found for global and direct radiation (Tables 5 and 6) and wind speed (Table 7). The quality of both satellite-derived radiation components is strongly affected by snow cover, which may be misinterpreted as clouds and radiation is subsequently underestimated. In addition, the density of surface stations used to correct inaccuracies in satellite-derived radiation is rather sparse, resulting in high CV errors. The low number of stations is compounded by difficulties in interpolating the spatially heterogeneous bias in global and direct solar radiation, and the strong influence of local topography (e.g. blocking of clouds). In the case of wind speed, this can be explained by the heterogeneity of the domain. Accordingly, the mesoscale wind field is modified by large gradients in wind speed from the coast towards inland locations, by topographical effects mainly in the German low

mountain ranges and in the Alps, and by the variability in local roughness lengths.

For hourly temperature prediction, errors are close to 1°C in all regions (Table 2). Regions with spatially complex terrain (mainly regions 4, 5 and 7) exhibit comparably larger errors during autumn and winter than the remaining regions, otherwise the errors are similar. A reason for this may be the higher frequency and intensity of valley-scale cold-pools during this time of the year (Hiebl and Frei 2015). CV errors of diurnal temperature range (Table 3) are greater and range from 1 to 2°C. This is because diurnal temperature range depends on both minimum and maximum temperatures, which are both more difficult to predict than hourly temperature.

The relative CV errors (regional CV error as compared to the region mean) for global radiation range from 7% in summer to 20% in winter (Table 5), with all regions exhibiting comparable relative errors. This is because regions with the highest radiation values also exhibit the greatest CV errors. For direct radiation (Table 6), the CV errors are generally higher than for global radiation and lie between 9% in summer and ~40% in winter. This can be explained by the higher inaccuracy of its retrieval and the lower station density compared to global radiation. Regions with lower direct radiation also exhibit overall larger relative errors.

The relative CV errors for wind speed (Table 7) range from 30 to 40%, with only minor differences between the regions. The relative CV is slightly higher in summer, due to lower average wind speed in this season. Hourly wind direction exhibits CV errors of between 30° and 50° (see Table 8).

Table 5 Relative RMSE (expressed in percent of the regional mean) for hourly mean global radiation and eight climate regions

Region	Jan	Feb	Mar	Apr	May	Jun	Jul	Aug	Sep	Oct	Nov	Dec
1	17	14	10	8	7	7	8	7	8	11	15	19
2	17	14	10	8	7	7	7	7	8	10	15	19
3	19	14	11	8	7	8	8	7	9	11	17	20
4	19	13	10	8	7	7	8	7	8	11	17	20
5	19	14	11	8	7	8	8	8	9	12	18	21
6	17	13	10	7	7	7	8	7	8	11	16	19
7	19	13	9	7	7	7	7	7	8	12	17	20
8	17	13	9	7	7	7	7	7	8	11	16	19

Table 6 Relative RMSE (expressed in percent of the regional mean) for hourly mean direct radiation and eight climate regions

Region	Jan	Feb	Mar	Apr	May	Jun	Jul	Aug	Sep	Oct	Nov	Dec
1	30	25	17	13	13	13	13	14	16	20	31	41
2	30	24	17	13	12	12	13	14	15	18	28	36
3	27	23	16	12	12	12	12	13	14	20	30	37
4	25	16	12	9	9	9	9	9	10	13	31	26
5	25	17	13	10	9	9	9	9	11	16	29	28
6	31	25	16	13	13	13	13	14	15	20	33	41
7	26	16	12	10	10	9	9	10	11	15	23	27
8	29	21	15	12	11	11	11	12	13	19	30	34

The larger errors in summer possibly result from the more frequent convective events which are influenced by the regional conditions and the highly variable wind directions (New et al. 1999; New et al. 2002). Moreover, thermally-driven winds (which are stronger in summer) are not resolved by the regional climate model CCLM. The errors detected for wind speed are comparable to those found in previous studies for other domains. Evaluations by New et al. (2002) revealed for monthly wind speed (using Thin Plate Splines interpolation) a RMSE (expressed in percent of the domain-mean) ranging from about 20% to over 60% depending on domain and season.

CV errors for SLP range from 0.6 to 3.0 hPa (Table 9), with significantly lower skill in regions of complex terrain. This indicates problems with data quality of observations in mountainous regions. Several formulas are available for the transformation of air pressure to sea level pressure, but all available formulas become more uncertain for higher altitudes.

For cloud cover, CV errors between 0.5 and 1.2 octa were detected (Table 10). The largest errors occur in winter due to snow cover which may be misinterpreted as clouds and will thus lead to an overestimation of cloud cover.

The relative CVs for down- and up-welling longwave radiation are between 3 and 7% (Table 11). Higher errors for down-welling longwave radiation occur where temperatures are low, and hence relative errors remain low in summer.

Evaluation of percentiles Although, relative prediction errors vary considerably for the climate variables, cross-validation

results show that the methods described in Sect. 3 overall consistently reproduce observed values across Germany (e.g. differences among the regions are small). Here, we consider the overall distribution provided by the cross-validation exercise and compare predicted with observed distributions. In Fig. Fig. 6a–i, examples are provided for predicted and observed empirical distribution functions (ecdf) for hourly variables and selected stations (or further details we refer to the figure caption).

Observed and predicted 2-m temperature (Fig. Fig. 6a) matches very well at the three evaluation stations, particularly the extremes that were well-reproduced. The slight underestimation at Aachen in the lower and middle part of the distribution function may be attributed to an underestimation of the urban heat island effect. The nearly perfect match at the mountain station (Feldberg) and the coastal station (Alte Weser) demonstrate the usefulness of the applied gridding method (non-linear temperature profile, non-Euclidian distance interpolation, coastal mountain).

Percentiles of relative humidity shown in Fig. Fig. 6b reveal an overestimation of up to 5% in the lower part of the distribution as compared with the observations. The mismatch of the observed and interpolated distribution in Aachen is linked to the simultaneously occurring underestimation of lower percentiles of 2-m temperature, while the dew point (not shown) is better reproduced. At the other stations, where relative humidity also tends to be overestimated, the mismatch relates to an overestimation of dew point temperature, while 2-m temperature is well reproduced.

Table 7 Relative RMSE (expressed in percent of the regional mean) for hourly wind speed and eight climate regions

Region	Jan	Feb	Mar	Apr	May	Jun	Jul	Aug	Sep	Oct	Nov	Dec
1	33	31	31	34	36	37	38	41	36	35	34	33
2	32	31	31	34	36	37	37	38	36	35	34	33
3	32	30	31	34	36	36	37	39	35	34	33	32
4	34	33	34	36	38	38	39	39	37	36	35	35
5	33	32	34	36	38	37	38	39	37	35	34	34
6	35	33	33	36	38	39	40	42	38	37	35	35
7	34	33	34	37	39	38	39	39	38	35	35	34
8	35	33	35	38	40	41	39	41	39	36	36	36

Table 8 RMSE (°) for hourly wind direction and eight climate regions

Region	Jan	Feb	Mar	Apr	May	Jun	Jul	Aug	Sep	Oct	Nov	Dec
1	37	36	39	45	48	48	49	50	45	41	39	36
2	34	34	37	43	45	46	45	47	42	38	36	35
3	35	33	37	44	46	46	47	48	42	38	36	34
4	35	33	37	43	45	47	46	47	43	38	35	33
5	34	34	38	44	46	47	47	48	44	39	36	34
6	37	35	39	46	48	48	49	50	45	40	39	36
7	34	33	37	44	46	47	47	48	43	37	34	33
8	35	34	37	45	47	48	47	49	44	38	36	35

According to Fig. Fig. 6c, SLP is very well reproduced for both evaluation stations, with a slight overestimation around the 50% percentile for Aachen (~1 hPa). Frequency distributions were only evaluated for low level stations, as only synop stations up to 600-m elevation were considered for the gridding.

The percentiles shown in Fig. Fig. 6d for Hohenpeissenberg (southern Bavaria) reveal and overestimation (underestimation) of the lower (higher) hourly radiation values as compared with the observations for January 1995–2012. In July, lower values are fairly well reproduced in the predictions, while the frequency of larger values is slightly underestimated. The mismatch of the observed and predicted distribution in winter can be attributed to snow cover which is misinterpreted as clouds in the satellite data. In summer, the spatial representativity of satellite- and station-based observations differs more strongly due to convective clouds, which may be the dominating factor for the inaccurate representation of extreme values. In all cases, the long-term averages are almost perfectly reproduced.

The percentiles of both the observed and the predicted SOL match well, particularly in January for the higher values (Fig. Fig. 6e). In winter, overestimation in the lower part of the distribution is primarily related to the occurrence of a snow cover. The surface emissivity, which strongly affects SOL, alters with the formation of a snow cover. The impact of snow on the surface emissivity is, however, not considered in CLM, which leads to increased uncertainty in the presence of snow. We decided not to correct for the impact of snow on SOL, as

the snow depth is only locally recorded and its interpolation would introduce further uncertainty. In July, lower (higher) percentiles of SOL are overestimated (underestimated) as compared with observations. The surface emissivity used to derive both the surface temperature at CCLM resolution and the SOL from down-scaled surface temperature at 1-km² resolution was derived from land type classes (Wilber et al. 1999) only. CCLM's surface emissivity, however, also depends on further parameters such as soil moisture. Hence, the calculated surface temperature slightly differs from the one used in CCLM, which triggers uncertainty in the down-scaling of surface temperature and as a consequence of the SOL.

At the three evaluation stations, the lower percentiles (~0–30% percentile) of predicted wind speed are by about 1 m/s higher than the observed ones (Fig. Fig. 6f). To some extent, this can be attributed to local effects at the stations and the technical specifications of the wind sensors (Vogt 1995). As a result of the friction force, very low wind speed (run-up velocity <0.3 m/s) cannot be detected by mechanic wind sensors, and friction force causes a general underestimation of low wind speeds (EURM 2000). Furthermore, station-based observations are only valid for their immediate environment. We accounted for roughness within the statistical down-scaling process (CORINE land use data) but kept it constant throughout the year and the study period (1995–2012). This may introduce some uncertainty into the gridded wind maps. Uncertainties may also be traced back to a less-than-ideal parameterization of the turbulence scheme and to non-

Table 9 RMSE (hPa) for hourly air pressure and eight climate regions

Region	Jan	Feb	Mar	Apr	May	Jun	Jul	Aug	Sep	Oct	Nov	Dec
1	0.8	0.6	0.6	0.6	0.7	0.6	0.6	0.6	0.5	0.5	0.5	0.5
2	0.8	0.6	0.6	0.6	0.6	0.6	0.6	0.6	0.5	0.5	0.5	0.5
3	1.2	1.1	0.9	1.2	0.8	0.9	0.7	0.8	0.7	0.7	1.0	0.9
4	2.7	2.9	3.0	3.0	2.9	2.8	2.9	2.8	2.9	2.4	2.5	2.3
5	1.8	1.5	1.2	1.5	1.1	1.3	1.1	1.1	1.0	0.9	1.3	1.2
6	1.1	0.9	0.8	0.9	0.9	0.8	0.8	0.8	0.8	0.8	0.8	0.8
7	2.0	1.1	1.1	1.3	1.1	1.1	1.1	1.1	1.1	1.0	1.1	1.1
8	1.9	1.4	1.2	1.5	1.1	1.1	1.0	1.1	1.0	1.0	1.4	1.2

Table 10 RMSE (1/8) for hourly cloud cover and eight climate regions

Region	Jan	Feb	Mar	Apr	May	Jun	Jul	Aug	Sep	Oct	Nov	Dec
1	0.9	0.7	0.6	0.6	0.5	0.5	0.5	0.5	0.6	0.6	0.8	0.8
2	0.9	0.7	0.7	0.6	0.6	0.5	0.5	0.5	0.6	0.6	0.8	0.8
3	0.9	0.8	0.8	0.7	0.7	0.6	0.7	0.6	0.7	0.8	1.0	1.0
4	1.2	1.0	0.8	0.9	0.9	0.8	0.7	0.7	0.8	1.1	1.3	1.3
5	1.2	1.0	0.9	0.9	0.8	0.7	0.7	0.7	0.8	1.1	1.3	1.3
6	0.9	0.7	0.6	0.6	0.6	0.5	0.6	0.6	0.6	0.7	0.9	0.8
7	1.2	0.9	0.8	0.7	0.8	0.7	0.6	0.6	0.7	1.0	1.2	1.2
8	1.1	0.9	0.8	0.7	0.7	0.6	0.6	0.6	0.7	0.9	1.1	1.1

resolved topographical structures (e.g. over-smooth surface) which particularly favours the overestimation of low wind speeds. Therefore, deviations between predicted and observed values should be interpreted with care.

For January 1995–2012, the SID distribution (Fig. Fig. 6g) for Hohenpeissenberg performs comparable to the SIS distribution, with a slightly more pronounced underestimation of lower percentiles. As for SIS, the underestimation of high SID values in January relates to snow-cloud misinterpretation. Also in July, SID performs comparable to SIS with a slightly more pronounced underestimation of larger values compared with SIS. The underestimation of the SID extremes in July can be attributed to the high spatial variability of cloud cover in summer. As a result of local shadowing effects of clouds and obstacles (e.g. orography, buildings, trees), shortwave radiation is highly variable in space and time, with SID in particular. For SIS, local effects are partially compensated as it constitutes the sum of direct and diffuse radiation.

The percentiles presented in Fig. Fig. 6h reveal a general underestimation of SDL values by 5–20 W/m², both in January and July. Main uncertainty sources are thereby the cloud correction factor (CCF) used to down-scale SDL and the clear-sky SDL (SDL_{cs}) which had to be estimated. CCF was derived by linear regression from CCLM data and is thus only valid in an average sense (regional variability not accounted for). Since SDL_{cs} was required for the down-scaling of SDL, yet not provided by CCLM, it was derived from water vapour content and air temperature using Eq. 3.7 (Sugita and Brutsaert 1993). We decided not to use ground-based observations for bias correction of the two longwave radiation datasets (SOL, SDL), as only few stations provide long-term observations. In addition, evaluations of ground-based longwave radiation observations revealed uncertainties

of up to 20 W/m², particularly during day time (Becker and Behrens 2012).

In general, the frequency distributions of observed and predicted wind direction match well (Fig. Fig. 6i). Deviations may be explained by site specific effects. While the CCLM model accounts for topographically induced effects (e.g. channelling effects), station-based observations are strongly affected by their immediate environment. Although interpolation of station-wise derived bias was performed accounting for orographic obstacles (e.g. relative elevation), further obstacles such as buildings and trees could not be taken into account but still may alter the frequency distribution of observed wind direction. Hence, a mismatch between predicted and observed frequency distributions should be interpreted with care.

4.2 Evaluation of the consistency in time and across variables

For the gridded data presented, observational time series from as many stations as possible that fulfil basic quality requirements were utilized. This approach results in a relatively high station density at any time and consequently improves the plausibility and accuracy of the resulting data grids. However, due to changes in the station network (e.g. stations are closed or newly opened), the possibilities of climatological analyses (e.g. the identification of long-term trends) are limited (Hiebl and Frei 2015). The focus is on temporal consistency over a day and on the consistency between variables, which is a key requirement of the TRY dataset. In this sub-section, we illustrate the consistency of the grids on a daily basis and across variables for a hot summer day (5.6.2003) with some convective activity (Fig. Fig. 8). As a reference, the general

Table 11 Relative RMSE (expressed in percent of the domain mean) for hourly down- (SDL) and up-welling (SOL) longwave radiation over the German domain

Region	Jan	Feb	Mar	Apr	May	Jun	Jul	Aug	Sep	Oct	Nov	Dec
SDL	7	7	6	6	5	4	3	4	5	6	6	7
SOL	4	3	3	3	4	3	4	3	3	3	3	3

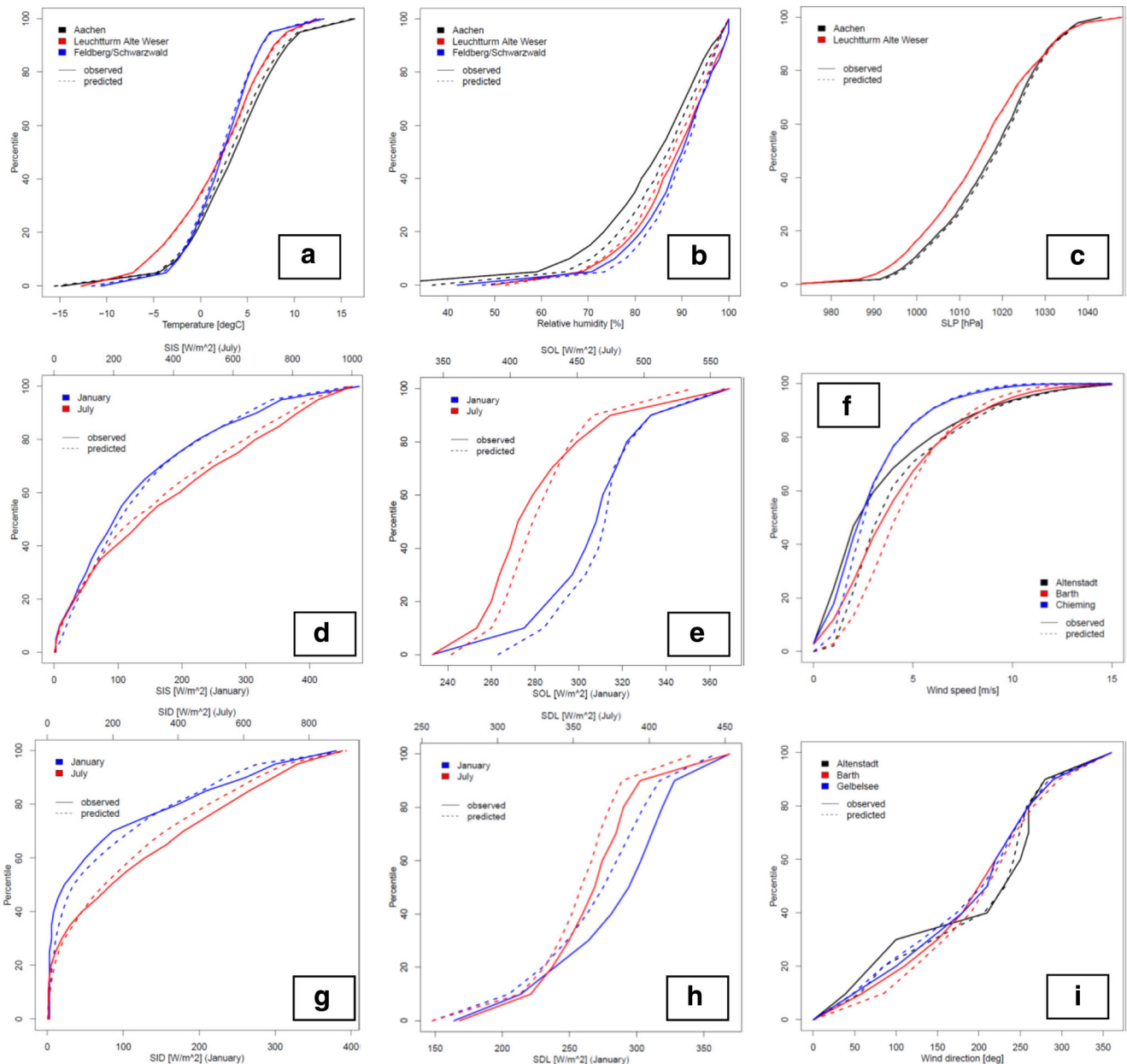


Fig. 6 Observed and estimated empirical distribution functions of hourly **a** 2-m temperature, **b** relative humidity, **c** sea level pressure, **d** global radiation (SIS), **e** outgoing longwave radiation (SOL), **f** wind speed, **g** direct radiation (SID), **h** downward longwave radiation (SDL) and **i** wind

direction over the period 1995–2012. The radiation parameters are given for January and July, SIS (**d**) and SID (**g**) at Hohenpeissenberg, SOL (**f**) and SDL (**h**) at Potsdam. For the remaining parameters, the evaluated stations are indicated by the figure legend

weather situation at 12 UTC is shown in Fig. Fig. 7 and in the following briefly described.

An occluded near-stationary frontal system crossing Germany is depicted in Fig. Fig. 7a. The frontal system belongs to an extensive low over the Atlantic. The pre-frontal situation is characterized by advection of unstable, warm air in a southwesterly flow with light surface winds of variable direction. Surface winds of prevailing easterly direction can be

seen over Bavaria and Erzgebirge with isolated local lows induced by thermal activity due to high solar radiation. Post-frontal subsidence occurs at the easterly wedge of the Azores high and is combined with reduced convective activity.

The synoptical weather reports (significant weather, cloud cover) in Fig. Fig. 7b also indicate the predominant occurrence of local thunder storms ahead of the frontal system along the German low mountain ranges of eastern and southern

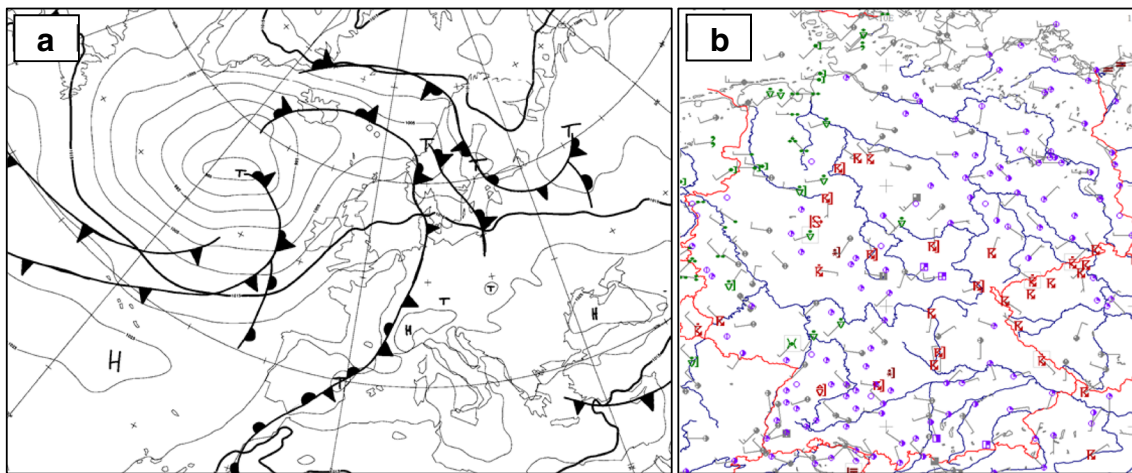


Fig. 7 a Surface analysis chart and b synoptical weather reports on 5.6.2003, 12 UTC

Germany. Further, thunder storms occurred along the frontal-system. Behind the front, high cloudiness or overcast sky dominated.

At 12 UTC (Fig. Fig. 8a–f), the air temperature exceeded 25°C in most areas of Germany and reached about 30°C across eastern Germany and Bavaria. Over north-western Germany, the air temperature was considerably lower and only reached 20°C as a result of a cold front which crossed Germany from the north-west. The air temperature decreased towards the coast and high elevations, particularly over the warmer eastern part of Germany. In consistence with the moving cold front, cloud cover was highest over north-western Germany, but it was also high in elevated areas due to orographic lifting.

In general, global radiation reached the highest values in areas where air temperature was also high, with gradually increasing values towards the south. The connection between cloud cover and global radiation can also be seen. Downwelling longwave radiation was high over western Germany, particularly in the upper Rhine Valley, where relatively high air temperatures, high cloud cover and high relative humidity occurred simultaneously.

Wind speed was highest along the frontal system and at the North Sea. Ahead of the frontal system, wind direction was variable with easterly winds in eastern Bavaria and near the Erzgebirge. Over north-eastern Germany and in the Rhine-Main Valley, the wind direction was overall westerly. The high variability of the wind direction ahead of the frontal system was in accordance to the isolated lows induced by thermal activity due to high solar radiation in the unstable air mass (see Fig. Fig. 7a).

At 15 UTC (Fig. Fig. 8g–i), thunderstorm cells formed over the western low mountain ranges triggered by the cold front moving across heated areas. In the areas of Nuremberg (northern Bavaria) and Goslar (southern lower Saxony), large thunderstorm clusters emerge. Strong winds and rainfall caused a

considerable drop in air temperature. Along the German coast, air temperature was less affected by the fast moving cold front, due to the mitigating effect of the sea.

Wind speed was again highest along the frontal system, at the North Sea and also in the vicinity of thunder cells. The wind direction was still variable ahead of the front. The wind direction markedly turned at the frontal system to north and behind the front eventually to west. In the Rhine–Main Valley, wind blew from the east resulting from a Taunus mountain range lee eddy.

4.3 Application examples

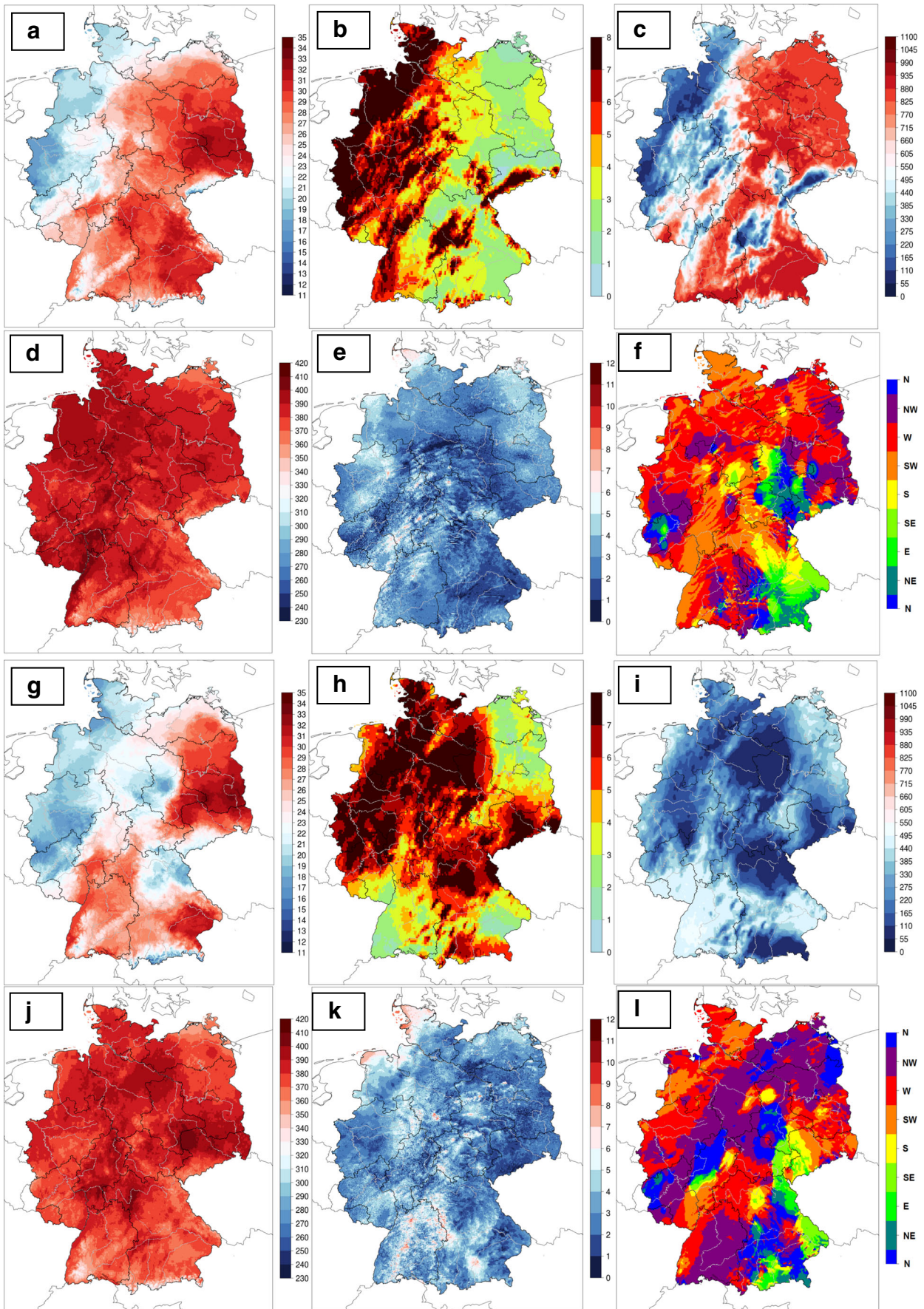
In this section, a selection of application examples is presented to demonstrate the usefulness of the gridded dataset. A complete graphical presentation is beyond the scope of this paper because of the enormous number of meteorological applications. Readers are referred to the Deutscher Wetterdienst for the download of the gridded dataset (NetCDF-4 format).

4.3.1 Temperature extremes

The annual number of summer days and frost days for two exceptional years (1996 and 2003) is calculated to illustrate the usefulness of the hourly temperature fields. Summer days (frost days) were determined on a grid-point-by-grid-point basis, counting all days where hourly temperature exceeds 25°C (falls below 0°C) at least once that day.

The resulting maps for summer days (Fig. Fig. 9) demonstrate the variability in counts in different years. In 1996 (a), the number of summer days was clearly lower compared to

Fig. 8 Air temperature [°C] (a, g), cloud cover [1/8] (b, h), global radiation [W/m²] (c, i), down-welling longwave radiation [W/m²] (d, j), wind speed [m/s] (e, k) and wind direction [°] (f, l), at 12 UTC (a–f) and 15 UTC (g–l) on 05.06.2003



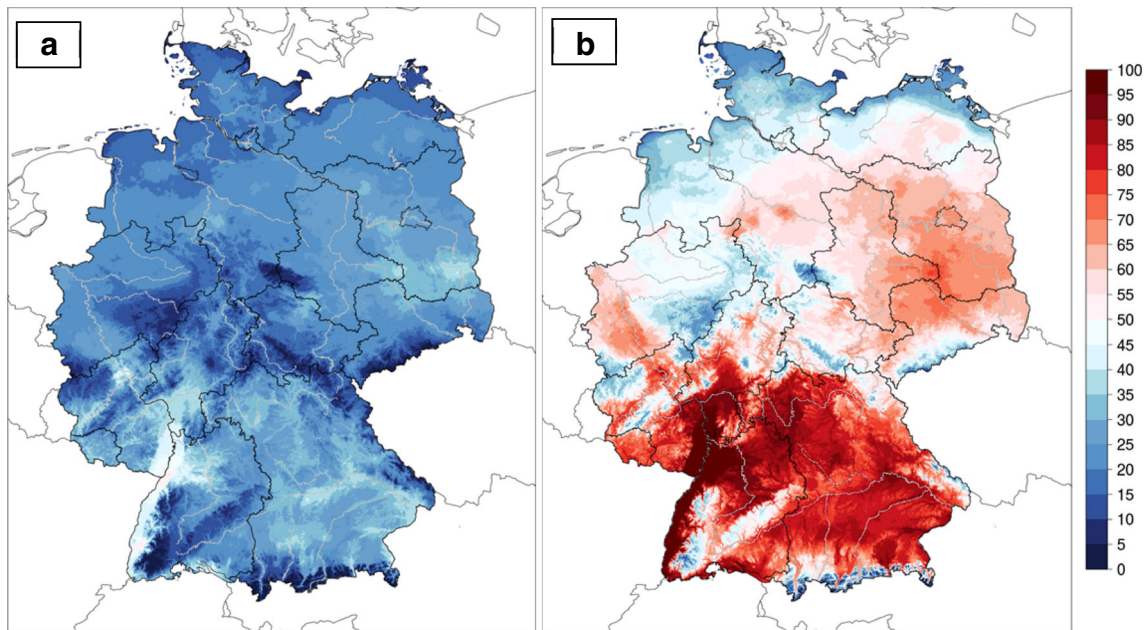


Fig. 9 Annual number of summer days, **a** 1996 and **b** 2003

2003 (b). Summer 2003 was the warmest in Germany since the beginning of nationwide measurements in 1881, while summer 1996 was the coldest on average over the period 1995–2012. In general, the effect of continentality is clearly visible, with considerably smaller numbers of summer days in coastal areas and over north-western Germany as compared to the eastern part. The highest number of summer days was reached in the upper Rhine Valley in southwestern Germany. The strong dependence of air temperature on elevation is also portrayed, with the least number of summer days in mountain

regions such as the Alps and the low German mountain ranges.

As with the summer days, the effects of continentality and elevation dependence are evident in the results for frost days in 1996 (Fig. Fig. 10a) and 2007 (Fig. Fig. 10b). The urban heat island (UHI) effect also clearly modifies the annual number of frost days. The annual mean air temperature within a large city can be more than 2°C higher than in nearby rural areas (e.g. Watkins et al. 2002). In the evening and at night, the UHI intensity can be much higher (as much as 10°C), as well

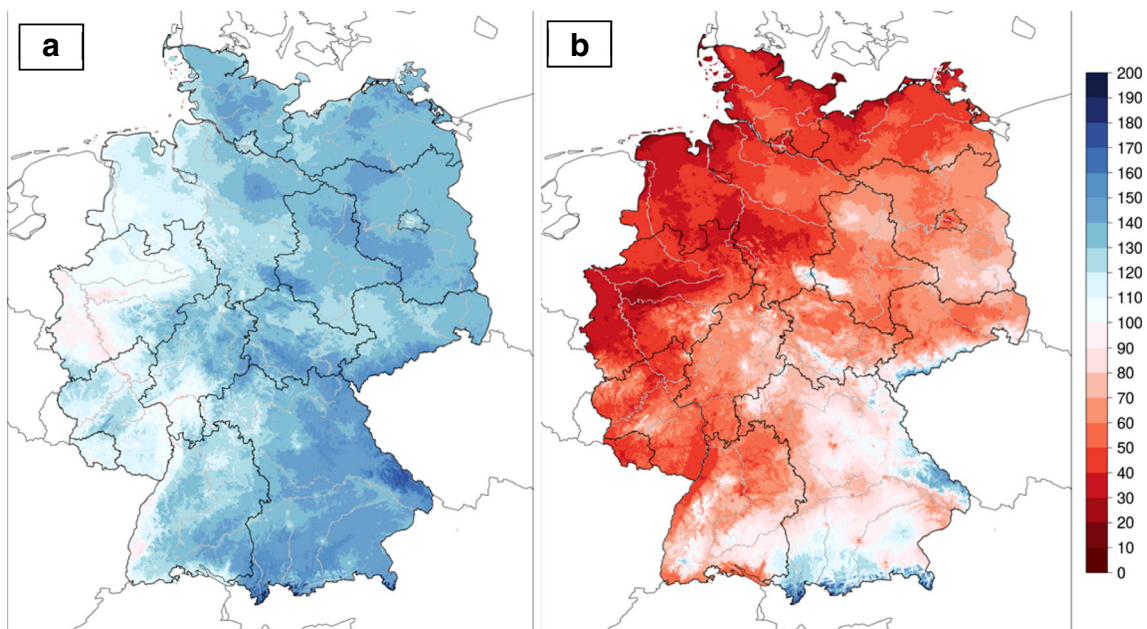


Fig. 10 Annual number of frost days, **a** 1996 and **b** 2007

as air temperature differences between city areas with different building structures (Buchholz and Kossmann 2015). The increase in minimum temperatures associated with UHI therefore means fewer and less severe frost events in cities. This is clearly depicted in Fig. Fig. 9a, b, where, for example, the cities in the Ruhr District, Berlin and Munich have considerably less frost days compared to surrounding areas.

4.3.2 Ninetieth percentile of hourly wind speed

Data from a regional climate model and some 150 wind speed stations throughout Germany contributed to the gridding of the wind dataset. The climate model simulation has captured general features of the wind field throughout Germany. The station data were used to correct biases inherent to the climate model simulation.

The general pattern of the 90th percentile of hourly wind speed is similar in winter (DJF; Fig. Fig. 11a) and summer (JJA; Fig. Fig. 11b) over the period 1995–2012. Nonetheless, the 90th percentile values are clearly higher in DJF (5–22 m/s) compared to JJA (3–15 m/s), particularly in the Erzgebirge and western Germany. The 90th percentile maps also depict several interesting features, including the north to south decrease in wind speed over the lowland plains and in mountain valleys, and the higher wind speed along the coast and on mountain ridges and peaks.

4.3.3 Annual sum of global radiation

Observations from 32 German ground stations were used to correct satellite-derived global radiation data. The most

significant adjustments were applied during the winter months and particularly relate to the snow-cloud misinterpretation inherent in satellite data.

Figure Fig. 12 presents the two most extreme years in terms of the annual total of global radiation in the period 1995–2012, namely 1995 (Fig. Fig. 12a) and 2003 (Fig. Fig. 12b). In 1995, the annual global radiation total was exceptionally low over southern Germany due to frequent west winds and increased cloud cover. In the upper Rhine Valley, the flatlands of Bavaria and eastern Germany, values of between 1120 and 1160 kWh/m² were reached, and in northern and western Germany 1000 and 1100 kWh/m². In the elevated areas, annual global radiation totals were generally below 1000 kWh/m². In 2003, the annual global radiation totals were above the climatological mean nationwide. Overall, it was a very warm, dry and exceptionally sunny year throughout Central Europe. The Sauerland, Harz and coastal regions received lower radiation total (1040–1200 kWh/m²) but with values still above the climatological mean. In regions south of the low German mountain ranges, the values exceeded 1300 kWh/m².

4.3.4 Perceived temperature

The RayMan bio-climate model (Matzarakis et al. 2010) was run in the Rhine-Main area with the gridded climate variables air temperature, relative humidity, global radiation and cloud cover, to obtain perceived temperature (Staiger et al. 2012) on 14.07.1995 at 5 UTC (Fig. Fig. 13a) and 12 UTC (Fig. Fig. 13b). Albedo and surface emissivity values were prescribed on the basis of the CLC land use data (following Pineda et al. 2002). The simulations were run in order to show the

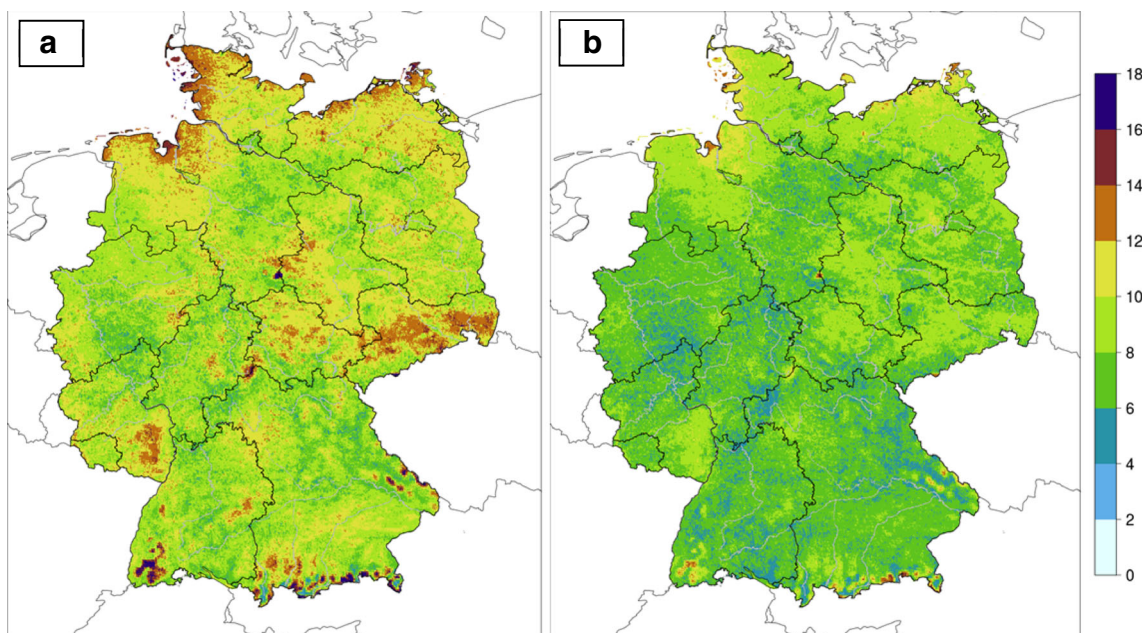


Fig. 11 Ninetieth percentile of hourly mean wind speed [m/s] over the period 1995–2012, **a** DJF and **b** JJA

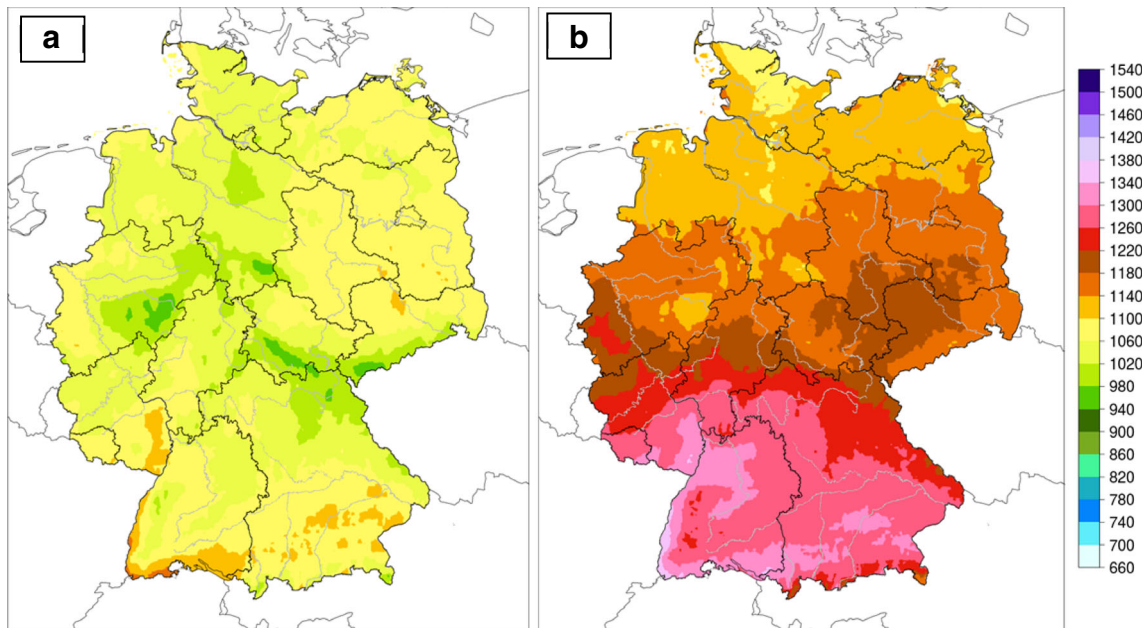


Fig. 12 Annual sum of global radiation [kWh/m^2] in **a** 1995 and **b** 2003

usefulness of the described dataset for applications in the framework of planning and health issues (Rosenfelder et al. 2015).

At 5 UTC, weather conditions were warm and humid in the Rhine-Main area. Early in the morning, air temperature was still high in urban areas ($>20^\circ\text{C}$) compared to the rural surroundings ($16\text{--}20^\circ\text{C}$) which can be attributed to the UHI effect. Elevated areas were also comparably warm due to a temperature inversion. Relative humidity was above 80% everywhere, and in the Frankfurt area, it was as high as 90%. Wind speed in most areas was lower than 1.5 m/s, except for the area around Donnersberg and on the ridges of the low mountain ranges. It is evident that in comparison with the

surrounding countryside, perceived temperature was considerably higher in urban areas with values of 20 to 24°C .

At 12 UTC, hot air temperatures of more than 30°C and low relative humidity ($<50\%$) prevailed in the Rhine/Main area with not much difference between the cities and the countryside. In the mountains, air temperature was considerably cooler, with an approximate lapse rate of $\sim 1^\circ\text{C}/100\text{ m}$ and relative humidity was higher ($\sim 70\%$). Wind speed was variable with values between 1 and 4.5 m/s, although lower in elevated areas. Global radiation was higher than 800 W/m^2 in most areas, but due to local cloud, some confined areas received less than 600 W/m^2 within 11–12 UTC. Some

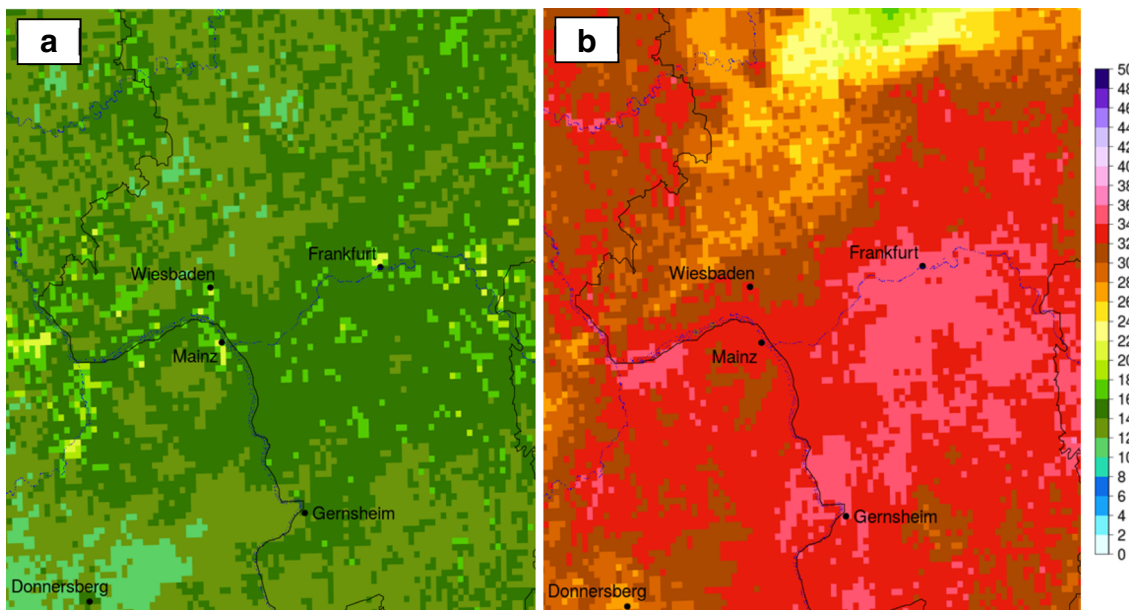


Fig. 13 Perceived temperature [$^\circ\text{C}$]: **a** 5 UTC and **b** 12 UTC on 14.07.1995

convective showers approached the region from the north and led to a decrease in air temperature ($<20^{\circ}\text{C}$) and an increase in relative humidity ($>80\%$). Perceived temperature was highest in the lowlands of the Rhine/Main area with hot spots of $\sim 40^{\circ}\text{C}$ around Frankfurt and Gernsheim (areas of high air temperature and low wind speed). In the mountains and over the north-eastern part of the Rhine–Main area, perceived temperature was considerably lower ($15\text{--}25^{\circ}\text{C}$).

5 Summary and conclusion

A high-resolution (1 km^2) gridded dataset of 12 hourly climate variables for Germany (covering the period 1995–2012) was created. The dataset is unique in terms of spatial and temporal resolution, and the number of contained variables. At present, the dataset comprises around 2,000,000 grids. It is available from the Deutscher Wetterdienst for scientific applications in various climate-related studies. It may also be used for hazard management, for the development of strategies for adapting to climate change or for the modelling of energy gain by solar and wind energy devices.

The dataset was derived from hourly station records that have been subject to manual and automated quality control. Values of poor or suspect quality have been removed. Only station records with valid data covering at least 5 years of the study period were used. In addition, satellite-derived data (cloud cover and short wave radiation components) and high-resolution downscaled reanalysis data using a regional climate model (longwave radiation and wind components) have been used. Gridding was done using the interpolation methods described in Sects. 3.1 to 3.7 which were individually designed, depending on available data sources and the physical properties of each climate variable. In addition, urban heat island (UHI) intensity was considered in the grids of air and dew point temperatures by linking it to CORINE land use classes, local weather conditions, time of the day and the season.

To achieve the highest possible precision in the data grids, interpolation was performed utilizing all available observational information that fulfils basic quality requirements. The results are inhomogeneities in the station network, which puts the long-term consistency of the dataset in question (Hiebl and Frei 2015). However, the focus is on temporal consistency over a day and on the consistency between variables, which is of high importance for the TRY dataset. Homogenized hourly station data were used when available. In addition, corrections were made for known station relocations, accounting for changes in coordinates, altitude and land use.

Cross-validation revealed the most accurate predictions for hourly air temperature, diurnal temperature range and hourly sea level pressure, followed by, in decreasing order, relative humidity, cloud cover, shortwave radiation, wind speed and

wind direction. Longwave radiation also seems to perform well. However, the few observing stations available do not allow for a thorough validation. Satellite-based cloud cover and shortwave radiation datasets perform worst from November to February, which can be attributed to variable snow cover that may be misinterpreted as clouds and subsequently leads to erroneous radiation values. Although in situ observations have been used to correct major inaccuracies in the satellite-derived data, the respective datasets should be used with care during the winter months and in areas of complex terrain.

To demonstrate the usefulness of the dataset presented for climate-related studies, some derived climate indices were presented at grid cell resolution. The number of summer days was exceptionally high in 2003, with over 100 days in the Rhine Valley. In 2007, the number of frost days was below 50 days in most of Germany, whereas in 1996, it was, on average, twice as high. Using the example of a hot day, perceived temperature was derived from the dataset for the Rhine–Main area. Early on this day, thermal loads were still high in cities which can be attributed to the UHI effect. At 12 UTC, perceived temperature was highest in low-lying regions close to the rivers Rhine and Main with values close to 40°C . Yet, due to convective activity, it was considerably lower in the north-eastern part ($<20^{\circ}\text{C}$) of the Rhine–Main area. The grids of global radiation and wind speed also showed high potential for further detailed studies. For example, the consistent provision of spatially and temporally highly resolved climatological information on global and direct surface solar radiation, temperature and wind speed allows an accurate estimation of PV potential in Germany including the efficiency under the given atmospheric conditions (Huld et al. 2013; Huld and Amillo 2015).

We have demonstrated that the newly developed high-resolution gridded dataset for Germany exhibits a wide range of performance skills. However, there are a few limitations in the gridded data, including inhomogeneities resulting from differences between station and satellite records and temporal variations in the station networks, smoothing out of extremes induced by interpolation, uncertainties inherent in the satellite-derived products and the reanalysis data and inaccurate representation of the urban heat island effect.

The user should be aware that over-smoothing is highly possible during the use of such datasets, as the impact of spatial interpolation on the magnitude of extremes is considerable (Haylock et al. 2008). A comparison based on cross-validation estimates revealed that higher percentiles (lower percentiles) tend to be under- (over-) estimated as a result of smoothing. For example, maximum energy yield will be affected by the underestimated higher percentiles of global radiation or wind speed.

Representativity of the wind data is also limited due to the course resolution ($2.8 \times 2.8\text{ km}^2$) of the DEM used by the

CCLM model. Topographically induced air flows such as channelling effects are only representative on the resolution of the underlying DEM.

Nevertheless, the gridded dataset presented contains a number of special features that make it highly suitable for use in climate and related activities. These include the following:

- It has been created using an extensive database, including station- and satellite-derived observations and model data.
- Gridding methods were designed depending on available data sources and the physical properties of each variable.
- It comprises 12 surface climate variables in hourly resolution.
- Datasets of air and dew point temperature also contain the urban heat island effect.

The dataset could be evaluated in further detail, for example, to identify areas and periods that contain values closer to the “truth” than others. The gridded dataset contains biases that need to be taken into account when evaluating climate models, for example, since mismatches between the modelled and the observed values may be partly explained by inaccuracies in the gridded data.

Acknowledgements The authors thank the Federal Institute for Research on Building, Urban Affairs and Spatial Development (BBSR) for the funding of the research project TRY. We are indebted to Klaus Keuler for providing the coarse-resolution COSMO-CLM runs. We thank Christoph Frei for helping to implement the calculation of the non-Euclidean distance fields and his helpful discussions that greatly contributed to improve the temperature grids. We thank Richard Müller, Uwe Pfeifroth and Anke Kniffka (DWD) for providing us with 18 years of hourly CM SAF SIS, SID, CAL and CFC for Germany. Special thanks are also given to the members of the Central Climate Office division at DWD for thematic discussions and to Thomas Gassdorf and Carsten Schwede for technical support. We thank Michael Kügler and Dagmar Berg at DWD for provision of station-based observations.

Open Access This article is distributed under the terms of the Creative Commons Attribution 4.0 International License (<http://creativecommons.org/licenses/by/4.0/>), which permits unrestricted use, distribution, and reproduction in any medium, provided you give appropriate credit to the original author(s) and the source, provide a link to the Creative Commons license, and indicate if changes were made.

References

- Alexandersson H, Moberg A (1997) Homogenization of Swedish temperature data. Part I: homogeneity test for linear trends. *Int J Climatol* 17:25–34
- Arakawa V, Lamb V (1977) Computational design of the basic dynamical processes in the UCLA general circulation model. In: Chang J (ed) *Methods in Computational Physics*, 17th edn. Academic Press, New York, pp. 174–264
- Baldauf M, Seifert A, Forstner J, Majewski D, Raschendorfer M, Reinhardt T (2011) Operational convective-scale numerical weather prediction with the COSMO Model: description and sensitivities. *Mon Wea Rev* 139:3887–3905. doi:10.1175/MWR-D-10-05013.1
- Becker R, Behrens K (2012) Quality assessment of heterogeneous surface radiation network data. *Adv Sci Res* 8:93–97. doi:10.5194/asr-8-93-2012
- Berg P, Wagner S, Kunstmann H, Schädler G (2013) High resolution regional climate model simulations for Germany: part I—validation. *Clim Dyn* 40:401–414. doi:10.1007/s00382-012-1508-8.
- Beyer HG, Costanzo C, Heinemann D (1996) Modifications of the heliosat procedure for irradiance estimates from satellite images. *Solar Energy* 56:207–212
- Blümel K, Hollan E, Kähler M, Peter R, Jahn A (1986) Entwicklung von Testreferenzjahren (TRY) für Klimaregionen der Bundesrepublik Deutschland. Bundesministerium für Forschung und Technologie. BMFT-FB-T86-051.
- Böhm U, Kucken M, Ahrens W, Block A, Hauffe D, Keuler K, Rockel B, Will A (2006) CLM—the climate version of LM: brief description and long-term applications. *COSMO Newsletter* 6:225–235 <http://www.cosmo-model.org>
- Buchholz S, Kossmann M (2015) Visualisation of summer heat intensity for different settlement types and varying surface fraction partitioning. *Landscape and Urban Planning* 144:59–64. doi:10.1016/j.landurbplan.2015.08.002
- Caesar J, Alexander L, Vose R (2006) Large-scale changes in observed daily maximum and minimum temperatures: creation and analysis of a new gridded dataset. *J Geophys Res* 111: D05101. doi:10.1029/2005JD006280
- Cannon DJ, Brayshaw DJ, Methven J, Coker PJ, Lenaghan D (2014) Using reanalysis data to quantify extreme wind power generation statistics: a 33 year case study in Great Britain. *Renewable Energy* 75:767–778
- Cano D, Monget JM, Albuissou M, Guillard H, Regas N, Wald L (1986) A method for the determination of the global solar-radiation from meteorological satellite data. *Solar Energy* 37:31–39
- Christoffer J, Deutschländer T, Webs M (2004) Testreferenzjahre von Deutschland für mittlere und extreme Witterungsverhältnisse (TRY). Deutscher Wetterdienst, Offenbach ISBN 3-88148-398-5
- Cros S, Albuissou M, Wald L (2006) Simulating Meteosat-7 broadband radiances using two visible channels of Meteosat-8. *Solar Energy* 80:361–367
- Daly C (2006) Guidelines for assessing the suitability of spatial climate data sets. *Int J Climatol* 26:707–721
- Dee DP, Uppala SM, Simmons AJ, Berrisford P, Poli P, Kobayashi S, Andrae U, Balmaseda MA, Balsamo G, Bauer P, Bechtold P, Beljaars ACM, van de Berg L, Bidlot J, Bormann N, Delsol C, Dragani R, Fuentes M, Geer AJ, Haimberger L, Healy SB, Hersbach H, Holm EV, Isaksen L, Kaallberg P, Kohler M, Matricardi M, McNally AP, Monge-Sanz BM, Morcrette JJ, Park BK, Peubey C, de Rosnay P, Tavolato TJN, Vitart F (2011) The ERA-Interim reanalysis: configuration and performance of the data assimilation system. *Q J R Meteorol Soc* 137:553–597. doi:10.1002/qj.828
- De Rooy WC, Kok K (2004) A combined physical-statistical approach for the downscaling of model wind speed. *Weather Forecast* 19:485–495
- Deutscher W (2008) Vorschriften und betriebsunterlagen nr. 3, beobachtungsbuch (BHB) 6.11. Offenbach am Main
- Doms G, Baldauf M (2011) A description of the nonhydrostatic regional COSMO model part 1: dynamics and numeric. Deutscher Wetterdienst, Offenbach <http://www.cosmo-model.org>
- Doms G, Förstner J, Heise E, Herzog H-J, Mironov D, Raschendorfer M, Reinhardt T, Ritter B, Schrodin R, Schulz J-P, Vogel G (2011) A description of the nonhydrostatic regional COSMO model. Part II: physical parameterization. Deutscher Wetterdienst, Offenbach <http://www.cosmo-model.org/>
- Dürr B, Schröder M, Stöckli R, Posselt R (2013) HelioFTH: combining cloud index principles and aggregated rating for cloud masking using infrared observations from geostationary satellites. *Atmos Meas Tech Discuss* 6:1859–1898

- EURM (2000) Messnetz 2000, automatische meteorologische Datenerfassung—AMDA III. Spezifikation der technischen Leistung—Pflichtenheft Software automatische meteorologische Datenfassungslage. EURM GmbH, Aachen
- Farr T, Rosen P, Caro E, Crippen R, Duren R, Hensley S, Kobrick M, Paller M, Rodriguez E, Roth L, Seal D, Shaffer S, Shimada J, Umland J, Werner M, Oskin M, Burbank D, Alsdorf D (2007) The Shuttle Radar Topography Mission. *Rev Geophys* 45:RG2004. doi:10.1029/2005RG000183
- Frei C (2014) Interpolation of temperature in a mountainous region using nonlinear profiles and non-Euclidean distances. *Int J Climatol* 34:1585–1605. doi:10.1002/joc.3786
- Frick C, Steiner H, Mazurkiewicz A, Riediger U, Rauthe M, Reich T, Gratzky A (2014) Central European high-resolution gridded daily data sets (HYRAS): mean temperature and relative humidity. *Met Z* 23(1):15–32
- Gandin L (1965) Objective analysis of meteorological fields. Israel Program for Scientific Translation, Jerusalem
- Gerth WP, Christopher J (1994) Windkarten von Deutschland. *Met Z* 3:66–77
- Geyer B, Weisse R, Bisling P, Winterfeldt J (2015) Climatology of North Sea wind energy derived from a model hindcast for 1958–2012. *J Wind Energ Ind Aerodyn* 147:18–29 <http://dx.doi.org/10.1016/j.jweia.2015.09.005>
- Goddard L, Mason S, Zebiak SE, Ropelewski CF, Basher R, Cane MA (2001) Current approaches to seasonal-to-interannual climate predictions. *Int J Climatol* 21:1111–1152
- Grasselt R, Schuettemeyer D, Warrach-Sagi K, Ament F, Simmer C (2008) Validation of TERRA-ML with discharge measurements. *Met Z* 17(6, Sp. Iss. SI):763–773. doi:10.1127/0941-2948/2008/0334
- Haylock MR, Hofstra N, Klein Tank AMG, Klok EJ, Jones PD, New N (2008) A European daily high-resolution gridded data set of surface temperature and precipitation for 1950–2006. *J Geophys Res* 113:D20119. doi:10.1029/2008JD010201
- Hengl T, Heuvelink GBM, Rossiter DG (2007) About regression-kriging: from equations to case studies. *Comput Geosci* 33:1301–1315
- Hermans A, Ament F, Geyer B, Matthias V, Quante M, Rockel B (2012) Evaluation of humidity, clouds and precipitation in COSMO-CLM and MM5 over Germany. *Met Z* 21(5):487–502
- Herrera S, Gutierrez JM, Ancell R, Pons MR, Frias MD, Fernandez J (2012) Development and analysis of a 50-year high-resolution daily gridded precipitation dataset over Spain (Spain02). *Int J Climatol* 32:74–85. doi:10.1002/joc.2256
- Hersbach H, Peubey C, Simmons A, Berrisford P, Poli P, Dee D (2015) ERA-20CM: a twentieth-century atmospheric model ensemble. *Q J R Meteorol Soc* 141:2350–2375. doi:10.1002/qj.2528
- Hiebl J, Frei C (2015) Daily temperature grids for Austria since 1961—concept, creation and applicability. *Theor Appl Climatol* 124(1):161–178. doi:10.1007/s00704-015-1411-4
- Hofstra N, New M (2009) Spatial variability in correlation decay distance and influence of angular-distance weighting interpolation of daily precipitation over Europe. *Int J Climatol* 29:1872–1880
- Holmes TRH, De Jeu RAM, Owe M, Dolman AJ (2009) Land surface temperature from Ka band (37 GHz) passive microwave observations. *J Geophys Res* 114:D04113. doi:10.1029/2008JD010257
- Huld T, Dunlop E, Beyer HG, Gottschalg R (2013) Data sets for energy rating of photovoltaic modules. *Solar Energy* 93:267–279
- Huld T, Amillo AMG (2015) Estimating PV module performance over large geographical regions. *Energies* 8:5159–5181
- Hutchinson MF (1998) Interpolation of rainfall data with thin plate smoothing splines: analysis of topographic dependence. *J G I D A* 2:168–185
- Jansen W, Sedlatschek R (2001) Ablauf der Datenprüfung und -vervollständigung im Geschäftsfeld Landwirtschaft. Deutscher Wetterdienst, Bericht 216, Offenbach
- Jarvis A, Reuter H, Nelson A, Guevara E (2008) Hole-filled seamless SRTM V4. Available from the CGIAR-CSI SRTM 90m Database. <http://srtm.csi.cgiar.org>
- Journel AG, Huijbregts CJ (1978) *Mining Geosciences*. Academic Press, London
- Källén E (1996) HIRLAM documentation manual—System 2.5. Swedish Meteorological and Hydrological Institute, Norrköping
- Karlsson GK, Riihelä A, Müller R, Meirink JF, Sedlar J, Stengel M, Lockhoff M, Trentmann J, Kaspar F, Hollmann R, Wolters E (2013) CLARA-A1: a cloud, albedo, and radiation dataset from 28yr of global AVHRR data. *Atmos Chem Phys* 13:5351–5367. doi:10.5194/acp-13-5351-2013
- Keil M, Bock M, Esch T, Metz A, Nieland S, Pfitzner A (2011) CORINE Land Cover 2006 - Europaweit harmonisierte Aktualisierung der Landbedeckungsdaten für Deutschland. Deutsches Zentrum für Luft- und Raumfahrt e.V. Deutsches Fernerkundungsdatenzentrum, Weßling <http://www.uba.de/uba-info-medien/4086.html>
- Kipp and Zonen (2004) Instruction Manual CM21 version 1004, Download centre, discontinued products. www.kippzonen.com
- Kljun N, Calanca P, Rotach MW, Schmid HP (2004) A simple parameterisation for flux footprint prediction. *Bound Layer Met* 112:503–523
- Koßmann M, Namyslo J (2007) Bestimmung effektiver aerodynamischer Rauigkeitslängen an Windmessstationen aus topographischen Karten (TK-Verfahren). Deutscher Wetterdienst, Offenbach
- Kotlarski S, Keuler K, Christensen OB, Colette A, Déqué M, Gobiet A, Goergen K, Jacob D, Lüthi D, van Meijgaard E, Nikulin G, Schär C, Teichmann C, Vautard R, Warrach-Sagi K, Wulfmeyer V (2014) Regional climate modelling on European scales: a joint standard evaluation of the ERO-CORDEX-RCM ensemble. *Geosci Model Dev* 7:1297–1333. doi:10.5194/gmd-7-1297-2014
- Kraehenmann S, Bissolli P, Rapp J, Ahrens B (2011) Spatial gridding of daily maximum and minimum temperatures in Europe. *Met Atmos Phys* 114:151–161. doi:10.1007/s00703-0311-0160-x
- Krähenmann S, Obregon A, Müller R, Trentmann J, Ahrens B (2013) A satellite-based surface radiation climatology driven by combining climate data records and near-real-time data. *Remote Sens* 5:4693–4718. doi:10.3390/rs5094693
- Krähenmann S, Walter A, Schettler-Köhler H, Pafferott J (2015) Constructive guidance. *International Innovation* 163:93–95
- Kuttler W, Weber S, Schonnefeld J, Hesselschwerdt A (2007) Urban / rural atmospheric water vapour pressure differences and urban moisture excess in Krefeld, Germany. *Int J Journal Climatol* 27:2005–2015
- Kysely J, Plavcova E (2010) A critical remark on the applicability of the E-OBS European gridded temperature data set for validating control climate simulations. *J Geophys Res* 115:D23118. doi:10.1029/2010JD014123
- Landelius T, Dahlgren P, Gollvik S, Jansson A, Olsson E (2016) A high-resolution regional reanalysis for Europe. Part 2: 2D analysis of surface temperature, precipitation and wind. *Q J R Meteorol Soc* 142:2132–2142. doi:10.1002/qj.2813
- Magnus G (1844) Versuche über die Spannkraft des Wasserdampfes. *Ann Phys Chem* 61:225
- Matzarakis A, Rutz F, Mayer H (2010) Modelling radiation fluxes in simple and complex environments: basics of the RayMan model. *Int J Biometeorol* 54:131–139. doi:10.1007/s00484-009-0261-0
- Mitchell KE, Lohmann D, Houser PR, Wood EF, Schaake JC, Robock A, Cosgrove BA, Sheffield J, Duan Q, Luo L, Higgins RW, Pinker RT, Tarpley JD, Lettenmaier DP, Marshall CH, Entin JK, Pan M, Shi W, Koren V, Meng J, Ramsay BH, Bailey AA (2004) The multi-institution North American Land Assimilation System (NLDAS): Utilizing multiple GCIP products and partners in a continental distributed hydrological modeling system. *J Geophys Res* 109:1–32 D07S90. doi:10.1029/2003JD003823

- Monin AS, Obukhov AM (1954) Basic laws of turbulent mixing in the ground layer of the atmosphere (Russian). *Tr Akad Nauk SSSR Geofiz Inst* 24(151):163–187
- Müller R, Trentmann J, Träger-Chatterjee C, Posselt R, Stöckli R (2011) The role of the effective cloud albedo for climate monitoring and analysis. *Remote Sens* 3:2305–2320. doi:10.3390/rs3112305
- Müller R, Pfeifroth U, Träger-Chatterjee C, Trentmann J, Cremer R (2015) Digging the METEOSAT treasure—3 decades of solar surface radiation. *Remote Sens* 7:8067–8101. doi:10.3390/rs70608067
- New M, Hulme M, Jones P (1999) Representing twentieth-century space-time climate variability. Part I: development of a 1961–90 mean monthly terrestrial climatology. *Amer Met Soc* 12:829–856
- New M, Lister D, Hulme M, Makin I (2002) A high-resolution data set of surface climate over global land areas. *Clim Res* 21:1–25
- Obukhov AM (1946) Turbulence in an atmosphere with a non-uniform temperature (Russian). *Tr Akad Nauk SSSR Geofiz Inst* 1:95–115
- Ohmura A, Gilgen H, Hegener H, Müller G, Wild M, Dutton EG, Forgan B, Fröhlich C, Philipona R, Heimo A et al (1998) Baseline Surface Radiation Network (BSRN/WCRP): new precision radiometry for climate research. *Bull Am Meteorol Soc* 79:2115–2136
- Ohmura A (2001) Physical Basis for the Temperature-Based Melt-Index Method. *J Appl Meteor* 40(4):753–761
- Oke T (1987) *Boundary Layer Climate*, 2nd edn. Routledge, London
- Peixoto JP, Oort AH (1996) The climatology of relative humidity in the atmosphere. *J Climate* 9:3443–3463
- Piper SC, Stewart EF (1996) A gridded global data set of daily temperature and precipitation for terrestrial biospheric modelling. *Global Biogeochem Cycles* 10(4):757–782
- Pineda N, Jorba O, Jorge J, Baldasano JM (2002) Using NOAA-AVHRR and SPOT-VGT data to estimate surface parameters: application to a mesoscale meteorological model. *Int J Remote Sens* 25:129–143
- Posselt R, Mueller R, Trentmann J, Stöckli R, Liniger M (2013) A surface radiation climatology across two Meteosat satellite generations. *J Geophys Res* 15:EGU2013–EGU7129
- Rhoades DA, Salinger MJ (1993) Adjustment of temperature and rainfall records for site changes. *Int J Climatol* 13(8):899–913 http://adsabs.harvard.edu/cgi-bin/nph-abs_connect?fforward=http://dx.doi.org/10.1002/joc.3370130807
- Ritter B, Geleyn JF (1992) A comprehensive radiation scheme for numerical weather prediction models with potential applications in climate simulations. *Mon Wea Rev* 120:303–325
- Rosenfelder M, Koppe C, Pfafferoth J, Matzarakis A (2015) Effects of ventilation behaviour on indoor heat load based on test reference years. *Int. J. Biometeorol.* 60:277–287
- Schär C, Davies TD, Frei C, Wanner H, Widmann M, Wild M, Davies HC (1998) Current Alpine climate. In: Cebon P, Dahinden U, Davies HC, Imboden DM, Jäger C (eds) *Views from the Alps: Regional perspectives on climate change*. MIT Press, Boston, pp. 21–72
- Senkler K, Streit U (2000) Anwendung einer offenen simulationsumgebung für atmosphärische prozesse eines diagnostischen strömungsmodells in atmogis. ASIM Mitteilungen 71, Wittmann J, Gnauck A, Page B, Wohlgemuth V (Hrsg.), Shaker Verlag, S. 43–52
- Spekat A et al (2011) Aktualisierte und erweiterte Testreferenzjahre von Deutschland für mittlere, extreme und zukünftige Witterungsverhältnisse. Deutscher Wetterdienst, Offenbach http://www.bbsr.bund.de/BBSR/DE/FP/ZB/Auftragsforschung/5EnergieKlimaBauen/2008/Testreferenzjahre/TRY_Handbuch.pdf;jsessionid=B3B40E57440401F2D32CB4CBD36D03CE.live!042?__blob=publicationFile&v=2
- Stahl K, Moore RD, Floyer JA, Asplin MG, McKendry IG (2006) Comparison of approaches for spatial interpolation of daily temperature in a large region with complex topography and highly variable station density. *Agr For Meteorol* 139:224–236. doi:10.1016/j.agrformet.2006.07.004
- Staiger H, Laschewski G, Grätz A (2012) The perceived temperature—a versatile index for the assessment of the human thermal environment. Part A: Scientific basics. *Int J Biometeorol* 56:165–176. doi:10.1007/s00484-011-0409-6
- Stappeler J, Doms G, Schattler U, Bitzer H, Gassmann A, Damrath U, Gregoric G (2003) Meso-gamma scale forecasts using the non-hydrostatic model LM. *Meteor Atmos Phys* 82:75–96
- Sugita M, Brutsaert W (1993) Cloud effect in the estimation of instantaneous downward longwave radiation. *Water Resour Res* 29:599–605
- Taylor PA (1987) Comments and further analysis on effective roughness lengths for use in numerical three-dimensional models. *Boundary Layer Meteorol* 39:403–419
- Tiedtke M (1989) A comprehensive mass flux scheme for cumulus parameterization in largescale models. *Mon Wea Rev* 117:1779–1800
- Uppala SM, Kållberg PW, Simmons AJ, Andrae U, da Costa BV, Fiorino M, Gibson JK, Haseler J, Hernandez A, Kelly GA, Li X, Onogi K, Saarinen S, Sokka N, Allan RP, Andersson E, Arpe K, Balmasada MA, Beljaars ACM, van de Berg L, Bidlot J, Bormann N, Caires S, Chevallier F, Dethof A, Dragosavac M, Fisher M, Fuentes M, Hagemann S, Hólm E, Hoskins BJ, Isaksen I, Janssen PAEM, Jenne R, McNally AP, Mahfouf JF, Morcrette JJ, Rayner NA, Saunders RW, Simon P, Sterl A, Trenberth KE, Untch A, Vasiljevic D, Viterbo P, Woollen J (2005) The ERA-40 re-analysis. *Q J R Meteorol Soc* 131:2961–3012
- Van den Besselaar EJM, Haylock MR, Van der Schrier G, Klein Tank AMG (2011) A European daily high-resolution observational gridded data set of sea level pressure. *J Geophys Res* 116:D11110. doi:10.1029/2010JD015468
- Vautard R et al (2013) The simulation of European heat waves from an ensemble of regional climate models within the EURO-CORDEX project. *Clim Dyn* 41:2555–2575
- Vogelsang R (1993) Plausibilitätskontrollen meteorologischer Daten. Deutscher Wetterdienst, Abschlussbericht des FE-Vorhabens, AMS-Nr. 90/08
- Vogt R (1995) Theorie, Technik und Analyse der experimentellen Flußbestimmung am Beispiel des Hartheimer Kiefernwaldes. Ein Beitrag zu den Energiebilanzuntersuchungen im REKLIP. stratus 3, Diss. Phil.- Nat.-Fak. Univ. Basel
- Wackernagel H (2003) *Multivariate geostatistics*. Springer, Berlin, Germany
- Walter A, Keuler K, Jacob D, Knoche R, Block A, Kotlarsk S, Müller-Westermeier G, Rechid D, Ahrens W (2006) A high resolution reference data set of German wind velocity 1951–2001 and comparison with regional climate model results. *Met Z* 15(6):585–596
- Watkins R, Palmer J, Kolokotroni M, Littlefair P (2002) The London Heat Island: results from summertime monitoring. *Building Serv Eng Res Technol* 23:97–106
- Wienert U, Kreienkamp F, Spekat A, Enke W (2013) A simple method to estimate the urban heat island intensity in data sets used for the simulation of the thermal behaviour of buildings. *Met Z* 22(2): 179–185
- Wieringa J (1986) Roughness-dependent geographical interpolation of surface wind speed averages. *Quart Journ Roy Met Soc* 111:867–889
- Wilber AC, Kratz DP, Gupta SK (1999) Surface emissivity maps for use in satellite retrievals of longwave radiation. NASA Langley Research Centre, Hampton
- Wild M, Ohmura A, Gilgen H, Roeckner E (1995) Regional climate simulation with a high-resolution GCM – surface radiative fluxes. *Clim Dyn* 11(8):469–286
- Will A, Woldt M (2009) Comparison of COSMO-CLM results with CM-SAF products: radiation components ToA, at the surface and cloud properties. IOP VS Study 16, Climate Monitoring Satellite Application Facility (CM-SAF) at DWD, Offenbach, Germany
- World Meteorological Organization (WMO) (1959) Values of some physical functions and constants used in meteorology. Technical regulations, basic doc. No. 2, WMO-No. 49 Vol. 1